Available online at www.sciencedirect.com

ScienceDirect

Geochimica et Cosmochimica Acta 292 (2021) 499–517

Geochimica et Cosmochimica Acta

www.elsevier.com/locate/gca

Primary crystallization and partial remelting of chondrules in the protoplanetary disk: Petrographic, mineralogical and chemical constraints recorded in zoned type-I chondrules

J. Pape [a,b,*], Å.V. Rosén [a], K. Mezger [a], M. Guillong [c]

[a] Institute of Geological Sciences, University of Bern, Baltzerstrasse 1+3, CH-3012 Bern, Switzerland
[b] Institut für Planetologie, University of Münster, Wilhelm-Klemm-Str. 10, 48149 Münster, Germany
[c] Institute of Geochemistry and Petrology, ETH Zurich, Clausiusstrasse 25, 8092 Zurich, Switzerland

Received 15 April 2020; accepted in revised form 15 October 2020; available online 22 October 2020

Abstract

Chondrules from unequilibrated ordinary chondrites are among the oldest Solar system materials and preserve mineralogical, chemical and isotopic signatures that link them to their primary formation mechanisms and environments in the early Solar System. Some chondrules record features indicating modifications by high- to low-temperature processes throughout their residence time in the protoplanetary disk. Chondrules that were partially modified after their primary formation record chemical, isotopic and textural information on their initial formation conditions and subsequent reprocessing that are essential to reconstruct their formation environments and interpret the ages recorded by individual chondrules correctly.

The detailed textural and major, minor and trace element analyses of two type-I chondrules from the low petrologic type ordinary chondrites MET 00526 and MET 00452 (L/LL3.05) reveal complex chemical and textural systematics bearing testimony of their multi-stage high temperature evolution, including reheating and partial remelting, in the evolving protoplanetary disk prior to accretion into their parent bodies. During primary crystallization of chondrule MET00526_Ch43, mineral growth, including incipient formation of feldspar in the outer parts of the chondrule, led to the fractionation of melt, eventually resulting in a chemical gradient in the mesostasis. During a later punctuated reheating that ultimately led to partial remelting of the outer parts of the chondrule, mesostasis and low-Ca pyroxene remelted partially. This partial remelting enhanced the chemical differences within the mesostasis and led to the formation of two chemically distinct mesostases in the inner and the outer zone of the chondrule with almost complementary abundances of Rb, Na, K, Ba, Sr and Eu. The calculated bulk mesostasis composition reveals chondritic relative abundances of these elements in the bulk chondrule with a slight depletion of the most volatile elements. Chemical and textural observations further indicate that this disequilibrium remelting occurred under more reducing conditions than the primary melting event preserved in the chondrule centre, allowing for the crystallization of a second generation of low-Ca pyroxene in the outer parts of the chondrule. Very similar processes are also recorded in chondrule MET00452_Ch22 with the degree of remelting being more extensive.

A previously determined young ^{26}Al-^{26}Mg age of ~3 Ma after CAIs determined for chondrule MET00452_Ch22 dates the time of the chondrule remelting rather than its primary formation. This is evidence for a late thermal event in the protoplanetary disk and generally indicates that multiple, distinct thermal pulses occurred in the chondrule forming region of the pro-

* Corresponding author at: Institut für Planetologie, University of Münster, Wilhelm-Klemm-Str. 10, 48149 Münster, Germany.
E-mail address: jonas.pape@uni-muenster.de (J. Pape).

https://doi.org/10.1016/j.gca.2020.10.019

toplanetary disk throughout the time of chondrule formation. The nonconcentric secondary outer zone around a spherical inner zone may indicate a directed heat source as the cause of partial remelting and reprocessing of primary chondrules.

Keywords: Chondrule formation; Chondrule remelting; Early solar system; Chondrule chronology

1. INTRODUCTION

Chondrules are solidified and partially crystallized melt droplets that formed between ~1.8 and ~3.0 Ma after the start of the Solar System defined by the formation of calcium-aluminum-rich inclusions (CAIs) by brief and intense melting events (e.g. Villeneuve et al., 2009; Pape et al., 2019). They are major components of unequilibrated ordinary and carbonaceous chondrites (UOCs and CCs) that escaped differentiation or intense metamorphism on their respective parent bodies, and are thus considered to sample some of the most pristine material from the beginning of the Solar System (Russell et al., 2018, and references therein). The mineralogical, chemical and isotopic records of chondrules are therefore considered as direct tracers of processes in the protoplanetary disk that played decisive roles in the formation and evolution of the early Solar System. However, the history of ~4.6 Ga old chondrules is complex and involves chemical and textural modification after primary formation that impacts on the interpretation of chondrule records, particularly the chondrule forming process and its physical and chemical conditions. Broadly three different environments can be defined in which significant modification of chondrules can occur and during which primary protoplanetary disk signatures recorded in chondrules can be altered or obliterated: (a) low- to high-temperature processing of chondrules in the protoplanetary disk, (b) low- to high-temperature (aqueous) alteration after accretion into parent bodies and (c) terrestrial weathering. The latter can be disregarded if meteorite falls are studied. Alteration of chondrules after accretion into their parent bodies is most obvious for highly metamorphosed type 4–6 chondrites, but even chondrules from unequilibrated type 3 chondrites experienced some low-temperature metamorphism on their parent bodies. For example, one of the least-metamorphosed ordinary chondrites Semarkona (type 3.00) has been heated to peak-metamorphic temperatures of ~260 °C on its parent body (Alexander et al., 1989). Further aspects of slight thermal metamorphism on the textural and chemical alteration of chondrules from type 3 chondrites and their implications for the modification of chondrules have been described in detail (e.g. Grossman and Brearley, 2005; Huss et al., 2006). In addition to incipient thermal metamorphism, low-temperature aqueous alteration of CCs and UOCs is widely documented (e.g.; Tomeoka and Buseck, 1990; Wasson and Krot, 1994; Sears et al., 1995; Rubin et al., 2007). These low-temperature modifications affected the meteorite samples as a whole and occurred after the chondrules had accreted on the respective parent bodies.

In contrast, some chondrules in unequilibrated type 3 chondrites show evidence for high-temperature modification that did not affect all chondrules and thus occurred prior to accretion into the parent body. These chondrules may have been reprocessed in the protoplanetary disk by high-temperature events during which they were heated above their solidus temperature, resulting in partial remelting of pre-existing chondrules. Textural and chemical observations that are controversially discussed as potential evidence for high-temperature reprocessing of chondrules include oxygen isotope systematics in compound chondrules (Akaki et al., 2007) and relict olivine grains (Ruzicka et al., 2007), igneous rims around chondrules, varying chondrule size distributions in different chondrite groups (Rubin, 2010), microchondrules embedded in fine-grained rims around larger host chondrules (e.g. Krot and Rubin, 1996; Krot et al., 1997) and the presence of compositionally distinct relict grains in both Fe-poor and Fe-rich chondrules (e.g. Jones, 1996; Ruzicka et al., 2008; Rubin 2010; Jones, 2012). Such evidence for high-temperature reprocessing (like relict grains) has been described for a wide range of chondrule types and chondrite groups, which indicates that the mechanisms leading to chondrule reheating either reoccurred in distinct regions of the protoplanetary disk at similar times or acted on a larger scale throughout the innermost protoplanetary disk. In either case, high-temperature processes seem to be important for the formation and subsequent textural, mineralogical and chemical evolution of chondrules.

The spread in apparent chondrule ages of at least 1–2 Ma in combination with the broad evidence for high-temperature reprocessing of chondrules has prompted several authors to discuss chondrule ages in the context of remelting (Kita et al., 2000; Bollard et al., 2017; Pape et al., 2019), although direct evidence is missing. If chondrules record complex formation and evolution histories involving re-occurring high-temperature events, the time constraints obtained by dating the formation of glass or mesostasis in single chondrules by internal isochron chronology may provide a spectrum of ages that reflects this dynamic process. Thus, the recognition and study of chondrule reprocessing using petrographic methods and geochemical observations has strong implication for the interpretation of high-resolution ^{26}Al-^{26}Mg ages obtained for individual chondrules (e.g. Villeneuve et al. 2009, Pape et al., 2019). However, later low-temperature (aqueous) alteration of chondrules can potentially obscure or diminish signatures relating to a former high-temperature modification process. The diversity of aqueous alteration and high-temperature reprocessing in distinct environments and during different times in the evolution of a chondrule can thus complicate the interpretation of chondrule textures and compositions and ultimately result in different

interpretations of similar observations (e.g. Matsunami et al., 1993; Grossman et al., 2002).

This study presents textural and chemical features from two Fe-poor chondrules from some of the least metamorphosed unequilibrated ordinary chondrites MET 00526 and MET 00452 that show evidence for partial high temperature processing of individual chondrules. The combined information from primary and secondary parts of individual chondrules provides a record of the process and the associated physical and chemical environment(s) during chondrule formation. A better understanding of the effects of reheating on the compositional modification of chondrules, of the heating process that led to chondrule remelting along with the timing of remelting will place firm constraints on the nature of high-temperature events and the dynamic evolution of the protoplanetary disk within the first few Ma of the Solar System.

2. MATERIALS AND METHODS

2.1. Samples

The samples selected for this study include two type-I (Fe-poor) IAB POP chondrules (after Hewins, 1997) from the ordinary chondrites MET 00526 and MET 00452 (both samples share many similarities and might be paired, although no such information is recorded in Meteoritical Bulletin Database). Sample MET 00526 has been studied in great detail by Grossman and Brearley (2005). Both samples are classified as L(LL)3.05 and are thus of the lowest metamorphic grade known from their respective parent body. Based on petrographic and chemical observations, the chondrules show similar types of modification after their primary formation. Mesostasis in chondrule MET00452_Ch22 displays continuous, radial chemical zoning in some major, minor and trace elements, while mesostasis in MET00526_Ch43 shows sharply delimited chemical compositions in the inner and outer part of the chondrule. Both chondrules contain two chemically distinct generations of low-Ca pyroxene that can be linked to two different melt generations. MET00452_Ch22 has been analysed for its Al-Mg systematic in a previous study (Pape et al., 2019).

2.2. Electron microprobe analysis

Major and minor element concentrations, chemical maps and secondary electron (SE) as well as backscattered electron (BSE) images were acquired by electron probe microanalyzer (EPMA) using a JEOL JXA-8200 Superprobe at the Institute of Geological Science, University of Bern. Some additional EMPA spot measurements were performed using a JEOL JXA-8530F HyperProbe at the Institute of Earth Sciences, University of Lausanne.

For EPMA the acceleration voltage was set to 15 kV with beam currents of 20 nA for quantitative spot analyses and 100 nA during acquisition of chemical maps. Well-characterized natural and synthetic silicate and oxide reference materials were used for calibration and an automated matrix correction was applied to the spot analyses using the built-in ZAF algorithm. The beam was focused to 1 μm for mapping and spot measurements of silicates and was defocused to achieve a diameter of 5–7 μm for measurements of mesostasis, attempting to minimize alkali loss. The X-ray background and peak intensities were measured for 15 and 30 s, respectively. The detection limit for Na was below 400 μg/g, the detection limits for all other elements were below 100 μg/g. X-ray intensity maps with a maximum resolution of 1024 × 1024 pixels were acquired by means of WDS with step sizes between 0.5 and 2 μm, depending on chondrule size and texture. Dwell times were set between 80 and 120 ms. The X-ray intensities of alkalis were always collected at the beginning of a measurement, i.e. measured in the first sequence of elements.

The X-ray intensity maps of Si, Mg, Fe, Al, Mn, Ti, Cr, Na, Ca and K were computed and transferred to background and density-corrected quantitative compositional maps using the XMapTools software (Lanari et al., 2014), which allows to standardize each pixel of a given X-ray intensity map using a set of quantitative spot analyses acquired prior to the mapping for each phase and element to be quantified. The EPMA spot measurements typically cause some local depletion of Na (and to a lesser degree K) in the mesostasis. This was accounted for during the quantification process of the X-ray intensity maps. The software also allows to attribute each pixel in the map to a distinct chemical phase, i.e. a mineral or mesostasis, based on compositional constraints and to compute and display standardized element maps for selected phases only (see e.g. Fig. 1). Densities of 3.3 g/cm^{-3} for olivine and pyroxene and 2.65 g/cm^{-3} for mesostasis were used to calculate density-corrected compositional maps. Phosphorus, Ni and S intensities were collected during mapping by means of EDS. The intensity data of these elements were not calibrated against standards and thus only used to better identify different mineral phases in the chondrules. Weathering veins in the two chondrules do not have any impact on the results of spot analyses as such areas were avoided during analysis. Additionally, pixels in the chemical maps associated to weathering features were eliminated during data processing using the XMapTools software.

2.3. Laser ablation SF-ICP-MS

Concentrations of lithophile trace elements in olivine, pyroxene and mesostasis were determined by Laser ablation sector field inductively coupled plasma mass spectrometry (LA-SF-ICP-MS) using an ASI Resolution 155 laser ablation system (wavelength 193 nm) coupled to a Thermo Element XR Sector-field ICP-MS at the Institute of Geochemistry and Petrology, ETH Zurich. Background and ablation times were ~30 s each with the laser energy set at 3.5 J cm^{-2} and a repetition rate of 5 Hz. Spot sizes were between 9 and 20 μm for mesostasis and between 13 and 30 μm for pyroxene and olivine. NIST 610 was used as primary reference material, bracketing blocks of typically 10–20 measurements of unknowns. Repeated measurements on the secondary reference material GSE-1G yielded an accuracy of better than 10% for rare earth elements (REEs). The SiO_2 concentrations in mafic silicates

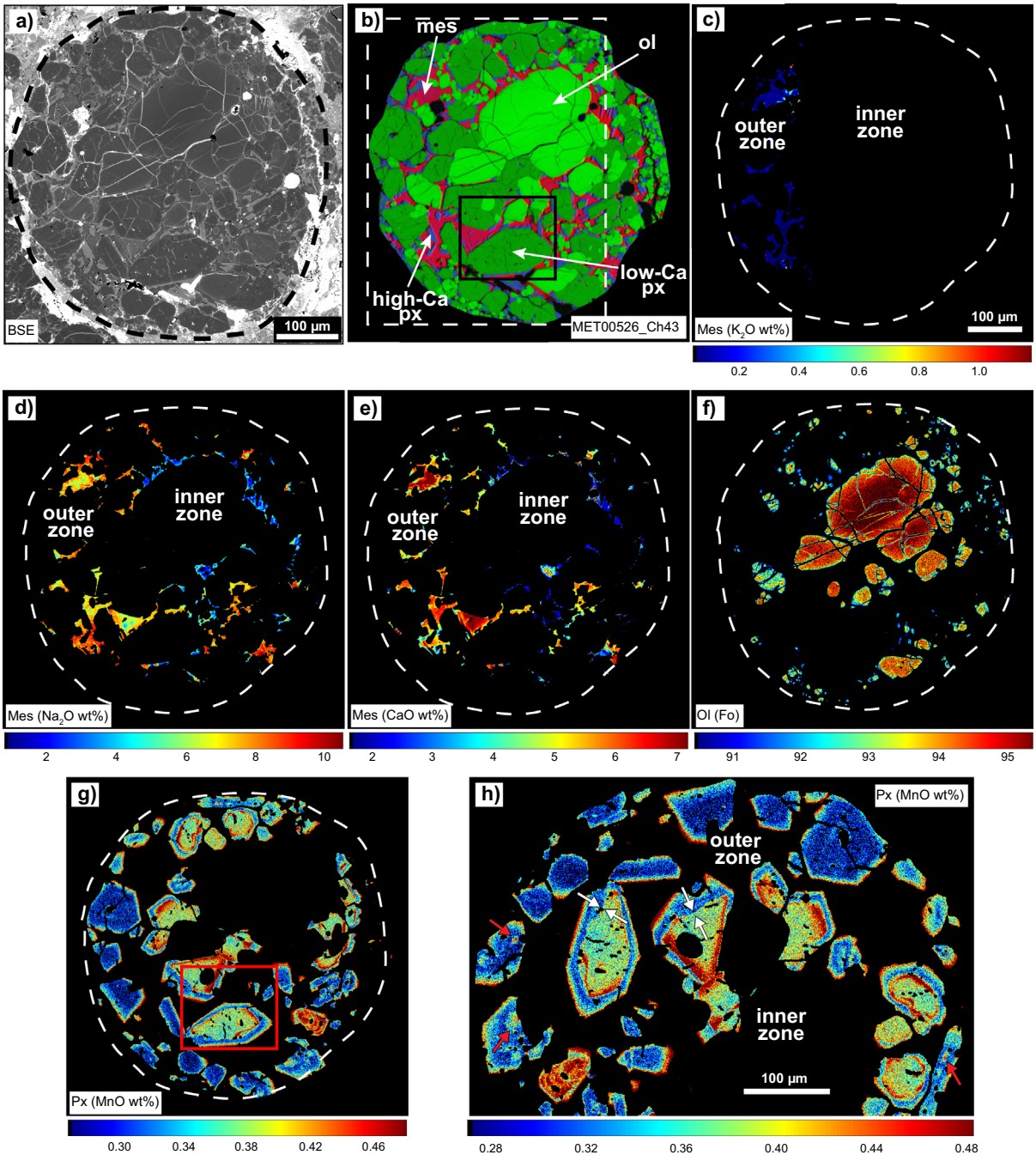

Fig. 1. Type-I chondrule MET00526_Ch43. (a) Backscattered electron (BSE) image, (b) Mg-Al-Ca composite image (dark-green = olivine (ol), light-green = low-Ca pyroxene (px), red = mesostasis (mes), blue = augite) and standardized element maps for (c) K_2O, (d) Na_2O and (e) CaO concentrations in mesostasis only (all other phases are masked-out from the maps). (f) Forsterite content in olivine. (g)–(h) Distribution of MnO (wt%) in low-Ca pyroxene. The map shown in (h) is an enlargement of (g), clockwise rotated by 90°. Dashed white lines in (c)–(g) indicate the outer limits of the chondrule. White arrows in (h) indicate areas where pyroxene gen-1 cores were partially resorbed. Compositionally distinct relict cores in pyroxene gen-2 are marked with red arrows (h). Black and red frames in (b) and (g) mark the area shown in the BSE image in Fig. 4a, the dashed white frame in (b) marks the area shown in (h). (For interpretation of the references to colour in this figure legend, the reader is referred to the web version of this article.)

and Al_2O_3 concentrations in the mesostasis, deduced from standardized EPMA element maps, were chosen for internal standardization (using the ^{29}Si and ^{27}Al intensities from LA-SF-ICP-MS). The LA-SF-ICP-MS data were processed as time-resolved signals using the SILLS program (Guillong et al. 2008). This allows to identify and exclude mesostasis measurements during which mineral phases like olivine and pyroxene, that were not visible prior to the analysis on the

sample surface, were ablated by using elements like Al, Fe and Ca as monitors.

3. RESULTS

3.1. Chondrule MET00526_Ch43

3.1.1. Major and minor element distribution

A BSE- and Al-Mg-Ca composite image (i.e. a phase map) as well as selected quantitative element maps for mesostasis, low-Ca pyroxene and olivine are shown in Fig. 1. Representative major and minor element concentrations of mesostasis, pyroxene and olivine are further presented in Tables 1–3. MET00526_Ch43 is a nearly round ~0.7 mm large magnesian type-I porphyritic olivine-pyroxene chondrule (Fig. 1a). Olivine occurs predominantly as subhedral phenocrysts (Fo 95) in the chondrule centre, as smaller sub- to euhedral crystals scattered in the mesostasis in the outer part of the chondrule (Fo 90–95) and as few poikilitic inclusions in low-Ca pyroxene (molar enstatite (En) 95, molar wollastonite (Wo) 0.5) (Fig. 1b). Low-Ca pyroxene is almost absent in the centre of the chondrule and homogeneously distributed throughout the rest of the chondrule and is, especially towards the chondrule rim, partly overgrown by augite (En 50–58, Wo 54–36) (Fig. 1b). The chondrule contains only minor amounts of metal and troilite, present as tiny blebs in the mesostasis and in silicates.

The mesostasis is homogeneously distributed throughout the chondrule (apart from the chondrule core that is dominated by large olivine crystals) and displays marked compositional zoning in the alkalis and Ca and to a lesser degree in Mn and Si (Fig. 1c-e, Table 1). Potassium is strongly enriched in the chondrule core (0.95 wt%) relative to the rim (0.02 wt%), whereas Na and Ca are relatively enriched in the chondrule rim (8 wt% and 6 wt%, respectively) and depleted in the core (0.5 and 1.9 wt%, respectively) (Fig. 1c-e). The mesostasis compositions amount to anorthite- and albite-dominated CIPW normative plagioclase compositions in the inner zone (henceforth mesostasis-1) and outer zone (henceforth mesostasis-2) of the chondrule, respectively (Supplementary Table S1, S2). Zonation of manganese in the mesostasis is less pronounced but is positively correlated with the zonation of Ca and Na. Silicon shows inhomogeneous distribution in mesostasis-2 and is slightly enriched in mesostasis-1. In some areas K, Na and Ca concentration trends might indicate a more gradual change from the inner to the outer parts of the chondrule, whereas sharp compositional transitions are observed in most areas of the chondrule (Fig. 1c-e). Mesostais-1 appears to be glassy in BSE images, whereas mesostasis-2 shows a feathery structure in some places (Fig. 2a-c). Aluminum, Fe and Ti concentrations show only very minor variations throughout the whole mesostasis, whereas Cr and Mg show a weak relative enrichment in mesostasis-1 over mesostasis-2 (Table 1). All mineral analyses give totals that are close to 100 wt%, but mesostasis-1 has systematically lower values. This could indicate the presence of light components that could not be measured by EPMA or be caused by an enigmatic analytical issue. Independent of the cause for the lower totals in mesostasis-1, normalizing all mesostasis analyses to 100

Table 1
Representative EPMA spot analyses of mesostasis (oxides in wt%) in zoned type-I chondrules.

SiO_2	Al_2O_3	MgO	K_2O	MnO	Cr_2O_3	Na_2O	CaO	TiO_2	FeO	Total
MET00526_Ch43										
Mesostasis-1										
62.80	19.87	1.76	0.83	0.37	0.04	0.47	2.04	0.53	5.44	94.15
63.58	18.34	1.95	0.79	0.24	0.13	0.24	2.50	0.57	5.02	93.36
64.09	18.33	3.70	0.86	0.34	0.14	0.62	1.89	0.62	4.86	95.45
67.16	19.65	1.47	0.95	0.33	0.36	0.63	1.75	0.57	3.05	95.92
Mesostasis-2										
61.28	19.85	0.91	0.04	0.37	0.04	7.69	5.64	0.35	2.61	98.78
61.91	18.83	0.96	0.07	0.36	0.08	8.15	5.77	0.47	2.29	98.88
62.13	19.61	1.16	0.03	0.23	0.05	8.72	4.63	0.38	1.55	98.48
58.99	17.80	1.16	0.02	0.63	0.05	6.83	6.76	0.50	4.29	97.02
58.74	19.02	1.19	0.02	0.42	0.03	7.29	6.38	0.40	3.46	96.94
57.74	18.75	1.09	0.03	0.42	0.03	6.93	6.14	0.35	4.65	96.13
62.69	17.81	1.09	0.03	0.35	0.08	8.34	5.64	0.52	2.25	98.80
MET00452_Ch22, *arranged by decreasing CaO*										
57.13	18.59	2.83	0.35	0.77	0.10	7.21	9.23	0.58	3.07	99.86
57.74	18.86	2.25	0.51	0.68	0.21	8.06	7.63	0.46	3.45	99.85
57.28	20.07	2.62	0.48	1.04	0.07	8.77	6.61	0.51	3.42	100.87
60.05	18.15	2.20	0.59	1.00	0.13	8.49	6.34	0.50	3.33	100.77
60.77	18.09	2.13	0.64	1.15	0.09	8.75	5.79	0.50	2.97	100.87
58.84	17.05	2.23	0.61	0.90	0.13	8.41	5.30	0.51	4.88	98.86
61.31	17.88	1.84	0.79	1.10	0.10	9.29	4.23	0.51	2.97	100.01
61.43	18.70	1.57	0.78	0.73	0.07	9.50	4.16	0.45	3.50	100.89
64.38	19.68	2.07	1.17	0.55	0.06	5.90	2.30	0.47	2.90	99.48
62.75	19.38	1.22	1.20	0.19	0.03	8.80	1.75	0.39	3.64	99.35

Table 2
Representative EPMA spot analyses of pyroxene (oxides in wt%) in zoned type-I chondrules.

SiO_2	MgO	Al_2O_3	MnO	Cr_2O_3	Na_2O	TiO_2	CaO	FeO	Total	Mg#	Wo#
MET00526_Ch43											
gen1											
58.71	36.13	0.20	0.29	0.49	0.00	0.04	0.20	3.14	99.21	95.4	0.4
58.35	35.33	0.21	0.41	0.60	0.01	0.05	0.18	3.62	98.76	94.6	0.3
59.07	36.14	0.14	0.35	0.51	0.00	0.02	0.24	3.04	99.52	95.5	0.5
59.02	36.60	0.20	0.29	0.48	0.01	0.03	0.22	3.22	100.06	95.3	0.4
58.94	36.42	0.23	0.34	0.51	0.02	0.03	0.26	3.04	99.79	95.5	0.5
57.90	34.40	0.49	0.46	0.66	0.04	0.07	0.32	4.12	98.50	93.7	0.6
57.81	35.21	0.57	0.46	0.90	0.05	0.06	0.37	3.67	99.13	94.5	0.7
58.44	36.13	0.28	0.38	0.77	0.00	0.04	0.30	2.98	99.31	95.6	0.6
58.06	36.42	0.23	0.32	0.63	0.00	0.03	0.24	2.93	98.86	95.7	0.5
gen2											
58.87	37.78	0.23	0.17	0.44	0.01	0.04	0.23	1.40	99.17	98.0	0.4
58.34	37.20	0.50	0.18	0.43	0.03	0.08	0.27	1.49	98.53	97.8	0.5
58.61	37.91	0.45	0.24	0.51	0.00	0.07	0.31	1.31	99.42	98.1	0.6
58.84	38.29	0.25	0.23	0.45	0.01	0.05	0.26	1.55	99.92	97.8	0.5
51.38	17.31	4.30	0.77	3.49	0.35	0.52	17.97	2.84	98.93	91.6	40.6
50.78	16.39	4.85	0.79	3.54	0.41	0.61	18.86	2.88	99.11	91.0	42.9
MET00452_Ch22											
58.42	36.77	0.35	0.44	0.69	0.01	0.04	0.29	2.68	99.70	96.1	0.5
58.99	37.87	0.25	0.33	0.55	0.00	0.03	0.21	2.44	100.67	96.5	0.4
59.00	37.59	0.11	0.25	0.45	0.01	0.02	0.17	2.21	99.82	96.8	0.3
58.86	37.68	0.22	0.31	0.52	0.00	0.03	0.18	2.27	100.06	96.7	0.3
59.15	37.38	0.17	0.30	0.53	0.02	0.04	0.19	2.39	100.17	96.5	0.3
59.19	37.44	0.21	0.26	0.48	0.01	0.04	0.17	2.38	100.19	96.6	0.3
58.59	37.08	0.26	0.31	0.54	0.00	0.04	0.18	2.34	99.35	96.6	0.3
48.57	15.40	7.33	1.49	3.50	0.17	1.10	19.27	2.64	99.47	91.2	45.1
50.90	19.77	5.10	1.59	3.08	0.20	0.57	15.19	3.06	99.47	92.0	33.7
49.46	16.51	6.18	1.05	2.94	0.15	0.97	18.88	2.57	98.71	92.0	43.0
51.30	17.70	4.78	1.46	2.64	0.22	0.68	18.58	2.38	99.75	93.0	41.2
50.57	16.01	5.40	1.73	2.90	0.23	0.78	19.53	2.31	99.47	92.5	44.8

Mg# = mol Mg/(mol Mg + mol Fe), Wo = Wo/(Wo + En + Fs).

wt% does not impact upon or change any interpretations and conclusions derived from the chemical data.

The olivine phenocrysts in the chondrule centre are mostly surrounded by K-enriched and Na- and Ca-depleted mesostasis-1. They are more magnesian (Fo 95) than the generally smaller olivine grains (down to Fo 90) that are in contact with Ca- and Na-enriched mesostasis-2 (Fig. 1f, Table 3).

Low-Ca pyroxene exhibits complex chemical zonation, which is most pronounced for Ca, Cr and Mn (Fig. 1g, h) and indicates, like the mesostasis, two distinct populations. Low-Ca pyroxene grains in the centre of the chondrule have chemically distinct cores (henceforth pyroxene gen-1), which are overgrown by ca. 10 μm-wide compositionally different rims (pyroxene gen-2). Pyroxene gen-1 cores are enriched in Cr and Mn and have systematically lower En contents (En 95) compared to the pyroxene gen-2 rims (En 98). Calcium, Cr and Mn concentrations throughout the rims (gen-2) are relatively constant but within individual mineral grains these elements increase at the grain edges. In contrast, in the pyroxene gen-1 these elements show gradual increase towards the core-rim boundaries that trace former mostly euhedral crystal faces. Some pyroxene gen-1 cores show discontinuous chemical zoning and embayments that are evidence of partial resorption prior to the formation of rims around pyroxene gen-1 (Fig. 1h). Manganese, Cr and Ca concentrations show the strongest zonation in pyroxene with concentrations similar in the outermost parts of both pyroxene generations. Low-Ca pyroxene phenocrysts in the outer part of the chondrule show homogeneous minor element concentrations throughout the grains. These clearly belong to gen-2 pyroxene since they have identical minor element concentrations (Mn, Cr) and En contents as the pyroxene-gen2 rims around pyroxene-gen1 in the chondrule centre. Some pyroxene-gen2 grains from the chondrule rim preserve tiny anhedral relict cores that are compositionally identical to pyroxene gen-1 and only visible in the detailed compositional maps shown in Fig. 1h.

3.1.2. Trace element distribution

Trace element concentrations of mesostasis and mafic silicates are presented in Table 4 and Fig. 3 a-b. Rare earth element (REE) patterns of mesostasis-1 and mesostasis-2 are close to chondritic and similar to each other ($1.0 \leq (Ce/Yb)_N \leq 1.6$) with REE contents between 10 and 20 × CI. However, while the Na- and Ca-enriched mesostasis-2 has positive Eu anomalies ($1.15 \leq Eu_N/Eu_N^* \leq 1.60$, with $Eu_N^* = (Sm_N + Gd_N)/2$), two measurements of K-enriched mesostasis-1 show negative Eu anomalies

Table 3
Representative EPMA spot analyses of olivine (oxides in wt%) in zoned-I chondrules.

SiO_2	MgO	MnO	Cr_2O_3	FeO	CaO	Al_2O_3	Total	Fo
MET00526_Ch43								
41.87	51.37	0.42	0.35	4.98	0.11	0.02	99.12	94.8
41.78	51.57	0.40	0.37	4.70	0.09	0.03	98.94	95.1
42.05	52.63	0.27	0.30	3.99	0.07	0.00	99.30	95.9
42.11	52.60	0.20	0.28	3.69	0.06	0.03	98.97	96.2
41.91	52.18	0.24	0.31	3.90	0.07	0.00	98.61	96.0
41.40	50.29	0.45	0.49	5.69	0.14	0.01	98.47	94.0
41.47	50.12	0.55	0.52	6.09	0.14	0.01	98.91	93.6
41.04	51.59	0.44	0.49	6.13	0.10	0.03	99.82	93.8
41.16	51.68	0.45	0.54	6.31	0.13	0.02	100.29	93.6
40.71	50.50	0.67	0.66	7.08	0.15	0.02	99.79	92.7
MET00452_Ch22								
41.62	52.88	0.43	0.55	4.27	0.12	0.02	99.89	95.7
41.77	53.49	0.37	0.47	3.81	0.08	0.01	100.00	96.2
41.85	53.38	0.37	0.44	4.02	0.06	0.03	100.14	95.9
41.83	53.41	0.38	0.45	3.94	0.06	0.03	100.10	96.0
41.63	52.72	0.51	0.66	4.71	0.13	0.01	100.38	95.2
41.61	52.55	0.49	0.52	4.43	0.14	0.02	99.76	95.5

($0.64 \leq Eu/Eu^* \leq 0.81$) and one analysis has a positive anomaly ($Eu/Eu^* = 1.24$). Negative and positive Eu anomalies in both types of mesostasis correlate with negative and positive Sr anomalies in the inner and outer mesostasis. Mesostasis-1 and mesostasis-2 have complementary abundances of Eu and Sr. Caesium is depleted in both types of mesostasis relative to other incompatible lithophile trace elements and shows significantly stronger depletion in mesostasis-2 ($0.3 \times CI$) as compared to mesostasis-1 ($1.2–1.4 \times CI$) (Fig. 3b). Similarly, Rb is strongly depleted in the mesostasis-2 ($0.2–0.6 \times CI$) relative to the mesostasis-1 ($8.3–8.9 \times CI$).

Pyroxene gen-2 is depleted in some trace elements like V, Sr and Hf in comparison to pyroxene gen-1 and shows enrichment of LREE and depletion of HREE relative to pyroxene gen-1, i.e. pyroxene gen-2 shows an overall flatter REE pattern with REE contents between 0.01 and $0.3 \times CI$ (Fig. 3a).

3.2. Chondrule MET00452_Ch22

3.2.1. Major and minor element distribution

A BSE- and Al-Mg-Ca composite image as well as quantitative element maps are shown in Fig. 4. Representative major and minor element concentrations of mesostasis and the mafic silicates are presented in Tables 1-3. MET00452_Ch22 is a slightly elongated 1.1 mm large type-I porphyritic olivine pyroxene chondrule, which shows a mineralogical zonation similar to the intermediate porphyritic low-FeO chondrules described by Scott and Taylor (1983). Anhedral to subhedral olivine occurs predominantly in the chondrule centre (Fo 96) and as few poikilitic grains enclosed in sub- to euhedral low-Ca pyroxene (En 96, Wo 0.3) towards the chondrule periphery (Fig. 4a). Augite occurs as overgrowth on some low-Ca pyroxene phenocrysts (Fig. 4a).

The mesostasis is homogeneously distributed throughout the chondrule and is concentrically zoned in Na, K, Ca, Si and Mn (Fig. 4), while Al, Mg, Fe, Cr and Ti concentrations do not show systematic trends. Na_2O concentrations increase from core to rim from 5.5 to 9.5 wt% and K_2O concentrations from 0.3 to 1.3 wt% (Fig. 4c). SiO_2 concentrations follow Na and K, whereas CaO is enriched in the core (9.2 wt%) and strongly depleted towards the rim (1.8 wt%) (Fig. 4d, e). MnO increases from core (0.6 wt%) towards the rim (1.2 wt%) and strongly decreases in the outermost 100–200 μm of the chondrule (0.2 wt%). Al_2O_3 and SiO_2 do not show systematic variations from core to rim, but display variable concentrations in different glass patches where they are generally anticorrelated.

Low-Ca pyroxene in MET00452_Ch22 shows a similar zonation as observed for pyroxene in MET00526_Ch43, although these chemical patterns are less prominent in MET00452_Ch22. Low-Ca pyroxene grains in the chondrule centre are systematically smaller than pyroxene grains in the outer part of the chondrule and display relict core areas with Ca and Mn enrichments, overgrown by rims that are relatively depleted in these elements. The larger euhedral low-Ca pyroxene grains towards the chondrule rim have homogeneous minor element contents throughout the grains with a steep increase of Mn, Cr and Ca towards the grain edges (Fig. 4f).

3.2.2. Trace element distribution

Trace element concentrations of mesostasis and mafic silicates are presented in Table 5 and Fig. 3c-d. The volatile elements Cs ($1.0–2.9 \times CI$) and Rb ($3.7–10.5 \times CI$) in the mesostasis are depleted relative to the other lithophile incompatible trace elements. Both elements correlate with Na and K and anticorrelate with the refractory Ca, while other incompatible lithophile trace elements, including the REEs, show no systematic trends from the inner zone to the outer zone, i.e. with decreasing Ca concentration (Fig. 3d). The REEs are enriched relative to CI ($La_N = 11–16$) and show mostly flat element abundance patterns with $1.1 \leq (Ce/Yb)_N \leq 1.6$. Some mesostasis

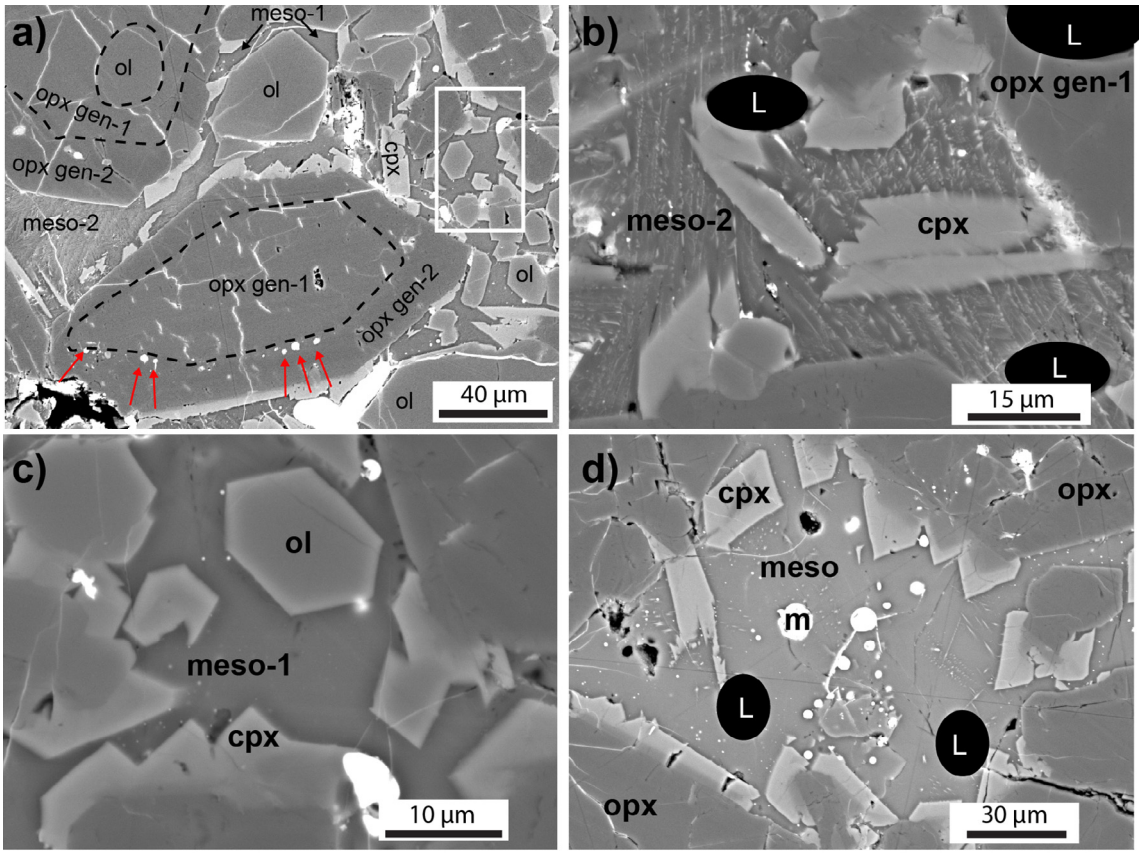

Fig. 2. Detailed BSE images of MET00526_Ch43 (a–c) and MET00452-Ch22 (d). Red arrows in (a) point at metal grains along the low-Ca pyroxene gen-1 (here opx-gen1) to low-Ca pyroxene gen-2 boundary (black dashed lines). Note the subparallel fibrous texture of mesostasis-2 (meso-2) in the triangular patch (left) in (a) and in (b). Mesostasis-1 (meso-1) shows a homogeneous glassy texture in (a) (black arrows) and (c). The white frame in (a) indicates the area shown in the close-up image in (c), rotated by 90°. The black circles (L) in (b) and (d) indicate locations of LA-ICP-MS measurements. ol: olivine; cpx: high-Ca pyroxene; m: metal. (For interpretation of the references to colour in this figure legend, the reader is referred to the web version of this article.)

measurements reveal small positive Eu anomalies whereas other analyses yield negative Eu anomalies that correlate with Sr anomalies. These anomalies do not correlate with major element zonation in the mesostasis. No systematic differences are observed between the element abundance patterns for the incompatible trace element analyses of mesostasis that show positive or negative Eu anomalies (Fig. 3d).

The REE contents in low-Ca pyroxene and olivine are similar (0.01–0.1 × CI). The LREEs are depleted relative to HREEs in pyroxene ($0.15 \leq (Ce/Yb)_N \leq 0.73$) as well as in olivine ($0.08 \leq (Ce/Yb)_N \leq 0.09$).

4. DISCUSSION

4.1. Partial remelting and primary differentiation of MET00526_Ch43

4.1.1. Low-Ca pyroxene

It has been reported previously that low-Ca pyroxene phenocrysts in type-I chondrules from UOCs show commonly only little overall chemical zoning (Jones, 1994). In the same study, only few low-Ca pyroxene grains in chondrules were found that recorded a decrease of FeO and some minor elements towards the grain edges. The improved capabilities of element mapping deployed in this study, including standardized element maps for minor elements like Mn, clearly reveal complex and discontinuous chemical zonation in low-Ca pyroxene. Some experimental studies, simulating rapid and single cooling histories of chondrules, report on complex chemical zoning in mafic minerals as the potential result of a single crystallization sequence (e.g. Pack and Palme, 2003). Additionally, oscillatory zoning in pyroxene and less commonly in olivine occurs in type-II and less frequently in type-I chondrules and is commonly interpreted to have been caused by crystal-melt disequilibrium effects during single heating and cooling events of chondrules (e.g. Jones, 1996, Marrocchi et al., 2018, Lewis and Jones, 2018), although some authors suggest that these patterns are evidence of multiple reheating (e.g. Baecker et al., 2017). The textural and chemical relationships and observations in MET00526_Ch43, however, strongly suggest that the two distinct low-Ca pyroxene generations crystallized from two distinct melts that did not co-exist at the same time. The chemical trends in the two different low-Ca pyroxene populations in MET00526_Ch43 (Fig. 1g, h, Table 2) (and likely MET00526_Ch22) indicate that both pyroxene

Table 4
Trace element concentrations in mesostasis and low-Ca pyroxene of chondrule MET00526_Ch43 determined by LA-ICP-MS.

		Mesostasis-1(centre)			Mesostasis-2 (rim)					Pyroxene gen-1			Pyroxene gen-2		
Al_2O_3 [a]	wt%	18.5	19.2	18.3	16.5	16.5	18.0	17.7	SiO_2 [a]	57.0	58.0	57.0	57.0	58.0	58.0
Sc	µg/g	23	14	22	28	32	13	16	µg/g	9.3	13	12	6.9	6.0	6.7
V	µg/g	17	6.4	18	29	29	2.7	11	µg/g	110	144	129	88	82	91
Rb	µg/g	20	20	19	1.1	1.4	0.98	0.99	ng/g	521	178	631	170	570	366
Sr	µg/g	38	48	34	117	98	150	106	ng/g	697	b.d.	1158	302	399	326
Y	µg/g	14	14	15	17	21	14	12	ng/g	94	122	120	95	49	77
Zr	µg/g	49	51	43	44	44	43	40	ng/g	116	239	223	61	118	129
Nb	µg/g	3.9	4.3	4.0	3.7	3.2	2.8	3.8	ng/g	14	24	49	15	47	39
Cs	µg/g	0.22	0.30	0.27	b.d.	b.d.	b.d.	0.064	ng/g	34	12	28	15	40	25
Ba	µg/g	26	28	25	33	39	28	38	ng/g	318	b.d.	287	b.d.	90	115
La	µg/g	3.3	3.7	3.5	3.3	3.8	3.1	3.1	ng/g	5.1	6.0	8.3	18.5	12.9	9.0
Ce	µg/g	7.7	8.2	8.6	8.7	9.1	7.2	8.3	ng/g	8.0	4.5	23	32	17	24
Pr	µg/g	1.1	1.1	1.3	1.2	1.5	1.0	1.1	ng/g	1.5	0.7	2.9	3.8	3.9	4.0
Nd	µg/g	4.9	5.6	5.4	5.9	7.2	5.7	5.5	ng/g	b.d.	5.6	9.4	21.7	8.4	b.d.
Sm	µg/g	1.3	1.4	1.6	2.2	1.6	1.8	1.5	ng/g	7.1	b.d.	8.9	0.0	b.d.	1.9
Eu	µg/g	0.40	0.69	0.42	0.86	0.77	1.1	0.73	ng/g	2.2	b.d.	5.5	b.d.	1.9	b.d.
Gd	µg/g	1.8	2.0	2.4	2.4	2.4	2.3	1.9	ng/g	b.d.	b.d.	b.d.	b.d.	b.d.	b.d.
Tb	µg/g	0.23	0.30	0.42	0.43	0.51	0.27	0.31	ng/g	1.6	1.6	b.d.	1.6	b.d.	0.8
Dy	µg/g	2.3	2.3	2.6	3.0	3.5	2.4	2.3	ng/g	11	16	19	15	11	13
Ho	µg/g	0.45	0.50	0.58	0.66	0.55	0.50	0.50	ng/g	5.2	4.7	5.8	3.7	2.3	5.3
Er	µg/g	1.4	1.5	1.7	1.9	2.7	1.8	1.5	ng/g	18	17	22	14	9	14
Tm	µg/g	0.21	0.23	0.23	0.26	0.35	0.27	0.18	ng/g	3.5	4.3	b.d.	b.d.	3.2	b.d.
Yb	µg/g	2.0	1.7	2.1	2.0	2.3	1.8	1.3	ng/g	25	30	35	16	13	10
Lu	µg/g	0.27	0.25	0.24	0.29	0.41	0.22	0.23	ng/g	3.7	6.1	8.1	3.7	3.4	4.6
Hf	µg/g	1.4	1.3	1.1	1.4	1.3	1.0	0.88	ng/g	6.7	11	14	1.0	4.8	2.5
Th	µg/g	0.45	0.47	0.36	0.32	0.38	0.32	0.39	ng/g	0.22	0.44	0.21	b.d.	b.d.	b.d.
U	µg/g	0.074	0.12	0.083	0.11	0.095	0.065	0.10	ng/g	b.d.	0.10	0.36	0.74	0.39	0.30

[a] Used for internal standardization, determined by EPMA; b.d. below detection limit.

populations grew from chemically distinct melts. The textural and chemical transition from low-Ca pyroxene gen-1 to low-Ca pyroxene gen-2 recorded in single pyroxene grains is not continuous but very sharp. It is recorded in major (Mg#), minor (Mn, Cr) and some trace elements (Zr, Hf, Sr, some REE), and is best documented for the incompatible element Mn (Fig. 1h) that shows truncation of the element zoning in the inner region. The embayments on the former crystal surface of some pyroxene-gen1 grains (Fig. 1 g, h) reveal that these crystals got partially resorbed before the new chemically different pyroxene-gen2 population grew. This clearly points towards a chemical disequilibrium between pyroxene-gen1 and the melt from which pyroxene-gen2 grew. Chemical observations and textural relationships furthermore show that pyroxene gen-2 grains in the outer part of the chondrule and the ~10 µm-wide pyroxene gen-2 rims around pyroxene gen-1 in the more inner part of the chondrule grew contemporaneously from the same melt. Whereas the two different low-Ca-pyroxene generations gen-1 and gen-2 must have crystallized from different melts. These observations suggest that the two melts were not coexisting as two distinct melts at the same time. The area in the chondrule in which low-Ca pyroxene gen-1 grains are overgrowth by low-Ca pyroxene gen-2 rims also broadly coincides with the boundary between mesostasis-1 and mesostasis-2. This indicates that both chemical and textural features are genetically related. Tiny compositionally distinct cores (of pyroxene gen-1 composition) in the outermost large low-Ca pyroxene gen-2 crystals additionally indicate remelting of low Ca-pyroxene.

Pyroxene gen-2 has higher Mg# compared to pyroxene gen-1, which indicates that both generations crystallized from melts with different Mg#. Reduction of FeO during partial remelting could have increased the Mg# of the melt from which the pyroxene gen-2 subsequently crystallized. As the Mg# in pyroxene gen-2 is only 3 mol% higher, reduction of FeO in the melt would not have had to be extensive, which is consistent with the observation that reduction of olivine (Jones and Danielson, 1997; Hewins et al., 2005; Ushikubo et al., 2013) is not observed in this sample. However, a single large metal bleb and additionally numerous tiny grains (confirmed to be metal by means of EDX) are disseminated in the mesostasis and within low-Ca pyroxene in the chondrule. While this is generally not unusual for Fe-poor chondrules, in MET00526_Ch43 small metal grains decorate the edges of olivine phenocrysts in the chondrule centre and occur within low-Ca pyroxene grains that record both generations of pyroxene growth. In some of these pyroxene grains, the metal blebs are aligned along the rim of pyroxene gen-1 and trace the transition between pyroxene gen-1 and pyroxene gen-2 (Fig. 2a). The Ni content of these metal grains could provide further information on their origin (i.e. primary chondrule metal vs. reduction product). Due to the small sizes of these grains, it was not possible to acquire reliable

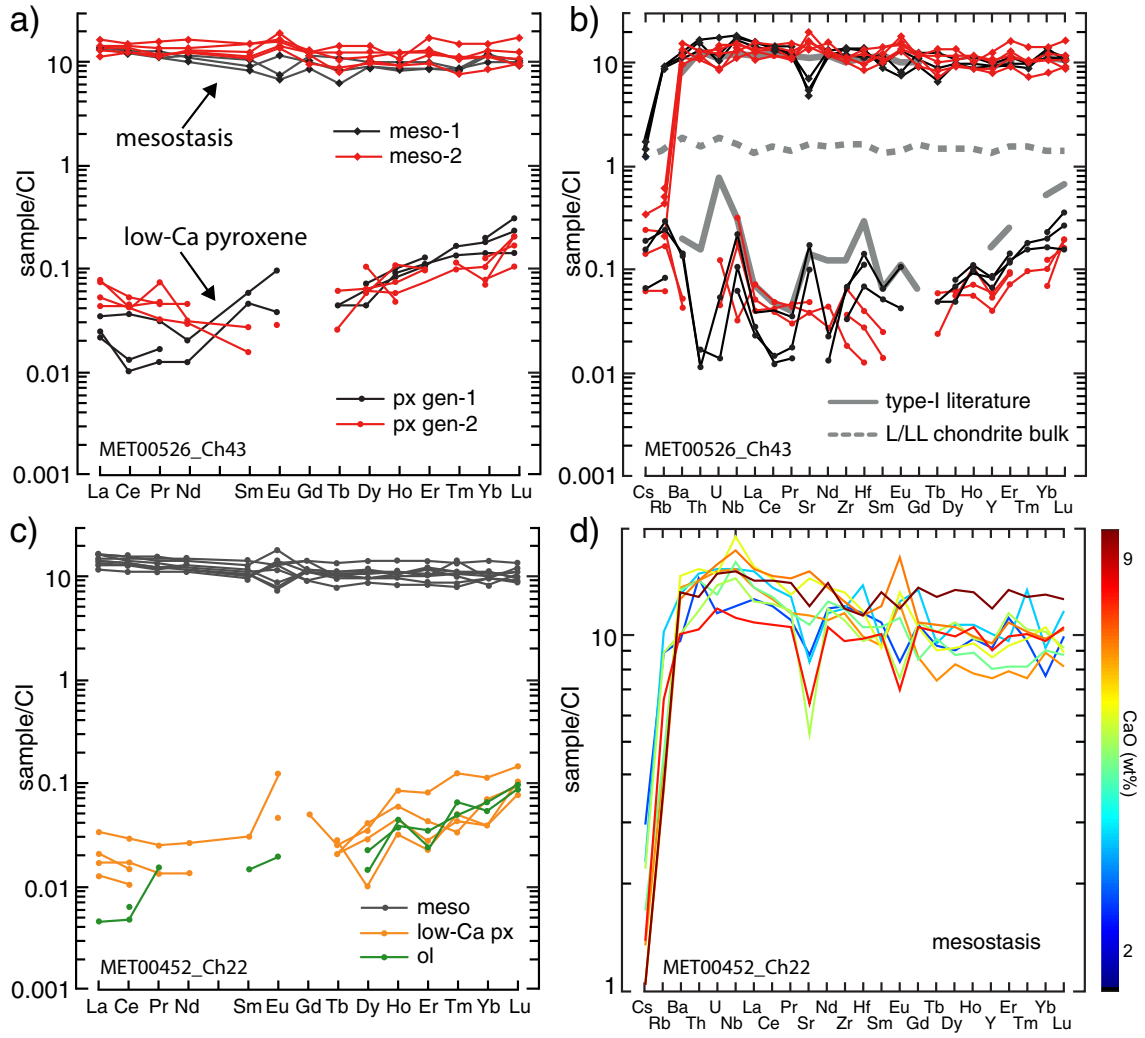

Fig. 3. CI-normalized (McDonough and Sun, 1995) rare earth element and lithophile trace element concentrations in mesostasis (meso), low-Ca pyroxene (px) and olivine (ol) of type-I chondrules MET00526_Ch43 (a–b) and MET00452_Ch22 (c–d). Average mesostasis and enstatite compositions for type-I chondrules (Jacquet et al., 2015) and average L/LL bulk chondrite compositions (Wasson and Kallemeyn, 1988) in (b) are shown for comparison. The colour code in (d) refers to the CaO concentration (wt%) in mesostasis, increasing from core to rim. (For interpretation of the references to colour in this figure legend, the reader is referred to the web version of this article.)

Ni concentration data. Nevertheless, semiquantitative EDX measurements yielded relatively low Ni contents mostly $\ll$5 wt% NiO, which further supports the reduction model. Combined, these observations indicate reduction of FeO concurrent with formation of a second melt. This reduction of FeO to Fe-meta required a reducing agent. Hanon et al. (1998) observed that carbon is generally more abundant in reduced type-I than in Fe-rich type-II chondrules. Additionally, experiments by Connolly et al. (1994) suggest that carbon might have plaid a significant role during formation of type-I chondrules. Although no C-phase has been observed in MET00526_Ch43, reduction could have been facilitated by the former presence of organic carbon or graphite in the sample. Alternatively, lower oxygen fugacity of the ambient nebular gas, i.e. nebular hydrogen, might have been sufficient for slight reduction of FeO in melt during partial remelting of MET00526_Ch43.

Disequilibrium between low-Ca pyroxene gen-1 and melt that eventually quenched as mesostasis-2 is further indicated by the resorption features along the former crystal faces of almost euhedral low-Ca pyroxene (white arrows in Fig. 1h) in the centre of the chondrule. These textures indicate only minor remelting of low-Ca pyroxene in the inner part of the chondrule. In contrast, only tiny relict cores, most likely of pyroxene gen-1 composition, can be observed in the large euhedral low-Ca pyroxene gen-2 grains in the outer part of the chondrule (red arrows in Fig. 1h). The rims of pyroxene gen-2 around pyroxene gen-1 in the inner part of the chondrule are only ~10 μm wide, but crystals of pyroxene gen-2 in the outer part of the chondrule are up to 200 μm in diameter.

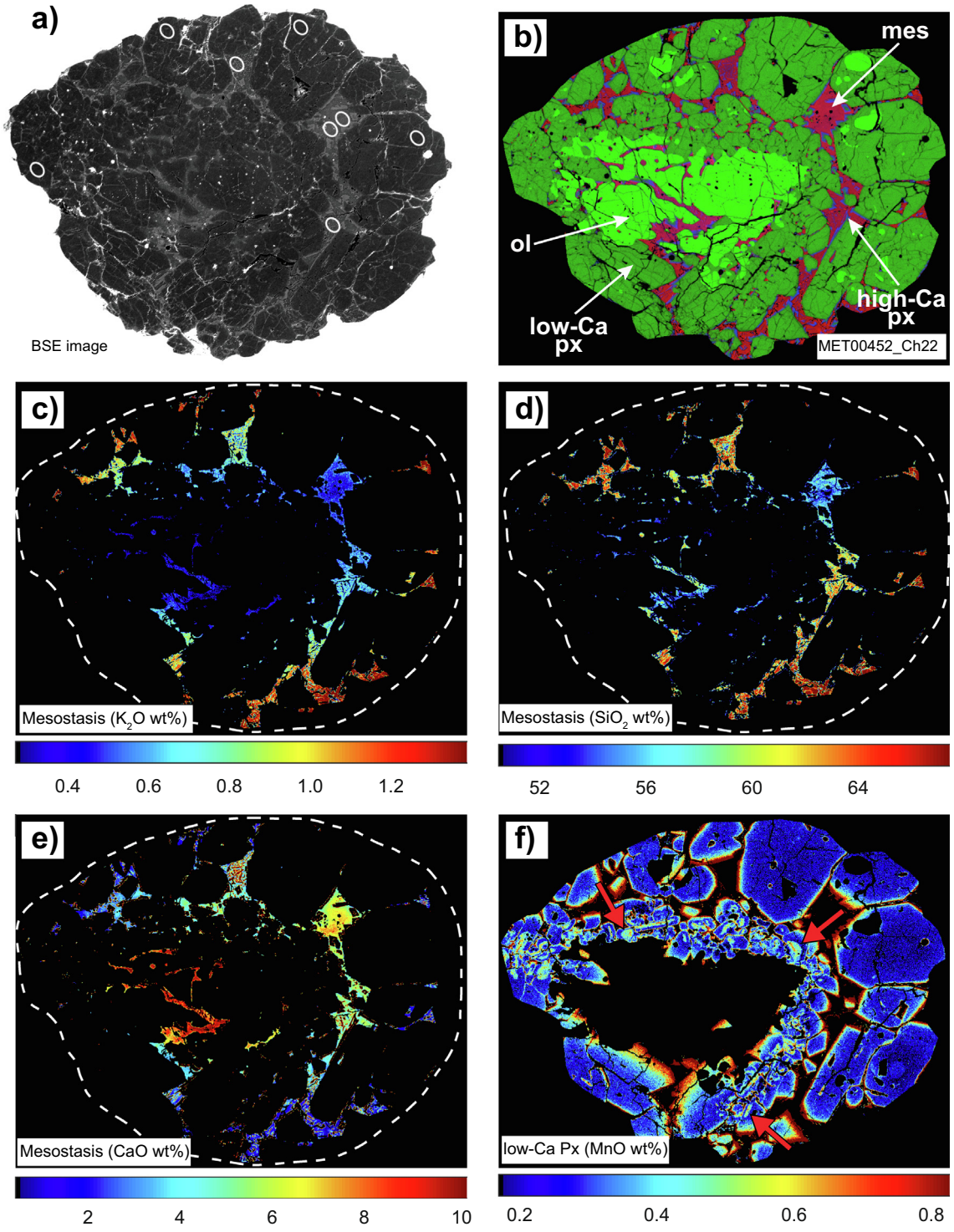

Fig. 4. Type-I chondrule MET00452_Ch22. (a) Backscattered electron (BSE) image. The white circles indicate locations where the chondrule has previously been analysed for Al-Mg isotopes (see discussion), (b) Mg-Al-Ca composite image (dark-green = olivine (ol), light-green = low-Ca pyroxene (px), red = mesostasis, blue = augite) and (c)–(e) standardized element maps of mesostasis only (all other phases are masked-out from the maps) for K_2O, SiO_2 and CaO concentrations, respectively. (f) Distribution of MnO (wt%) in low-Ca pyroxene. Red arrows in (f) point to chemically distinct relict cores in low-Ca pyroxene. Dashed white lines indicate the outer limits of the chondrule. (For interpretation of the references to colour in this figure legend, the reader is referred to the web version of this article.)

Combined, all these observations are not consistent with a single crystallization event but reveal partial remelting that was highest towards the chondrule periphery but minor towards the centre. This in turn implies a high

Table 5
Trace element concentrations in mesostasis, low-Ca pyroxene and olivine of chondrule MET00452_Ch22 determined by LA-ICP-MS.

		Mesostasis										Pyroxene				Olivine	
Al_2O_3[a]	wt%	17.5	17.5	18.0	18.0	17.5	19.0	18.0	15.0	13.0	SiO_2[a]	56.5	56.5	56.5	56.5	40.0	40.0
Sc	µg/g	16	20	8.3	9.1	23	12	18	34	36	µg/g	4.3	5.5	2.9	3.0	2.5	2.9
V	µg/g	3.0	6.5	2.7	3.8	13	2.6	6.6	66	38	µg/g	71	80	63	62	71	90
Rb	µg/g	21	24	10	11	21	8.9	8.5	15	8.7	ng/g	147	319	27	429	5.1	b.d.
Sr	µg/g	65	62	85	80	39	108	113	47	90	ng/g	518	647	90	1787	b.d.	b.d.
Y	µg/g	14	16	12	13	15	14	15	15	19	ng/g	46	85	28	48	38	41
Zr	µg/g	48	47	46	47	44	52	49	38	47	ng/g	49	44	28	54	17	21
Nb	µg/g	3,0	3.8	3.8	3.9	3.6	4.7	4.3	2.8	3.8	ng/g	15.9	14.3	8.6	23.6	5.7	7.2
Cs	µg/g	0.56	0.44	0.25	0.32	0.42	0.20	0.13	0.26	0.12	ng/g	b.d.	15.3	b.d.	21.7	b.d.	b.d.
Ba	µg/g	23	33	34	34	25	36	32	25	33	ng/g	b.d.	152.2	b.d.	881.2	b.d.	b.d.
La	µg/g	3.1	3.7	3.3	3.4	3.0	3.8	3.8	2.7	3.5	ng/g	b.d.	3.7	2.7	7.4	1.0	b.d.
Ce	µg/g	7.7	8.7	8.0	8.2	7.7	9.2	9.3	6.8	9.0	ng/g	8.2	9.8	5.7	16.7	2.8	3.5
Pr	µg/g	1.0	1.2	1.1	1.1	1.1	1.2	1.4	1.0	1.4	ng/g	b.d.	1.1	b.d.	2.2	1.4	b.d.
Nd	µg/g	5.6	5.4	5.2	5.9	5.6	6.4	6.5	4.9	6.7	ng/g	b.d.	5.5	b.d.	11.4	b.d.	b.d.
Sm	µg/g	1.7	1.5	1.4	1.6	1.5	1.4	1.9	1.5	2.0	ng/g	b.d.	b.d.	b.d.	4.3	b.d.	2.1
Eu	µg/g	0.49	0.73	0.71	0.65	0.44	0.77	0.98	0.40	0.69	ng/g	2.3	b.d.	b.d.	6.6	b.d.	1.1
Gd	µg/g	2.2	2.7	1.8	1.7	2.2	2.2	2.2	2.2	2.8	ng/g	b.d.	9.3	b.d.	b.d.	b.d.	b.d.
Tb	µg/g	0.35	0.35	0.27	0.36	0.38	0.34	0.40	0.38	0.48	ng/g	0.7	0.8	0.9	0.7	b.d.	b.d.
Dy	µg/g	2.3	2.7	2.1	2.2	2.7	2.3	2.7	2.5	3.4	ng/g	9.6	7.9	2.2	6.6	3.6	5.7
Ho	µg/g	0.55	0.60	0.44	0.50	0.55	0.53	0.56	0.59	0.74	ng/g	3.2	4.4	1.6	2.3	2.5	2.1
Er	µg/g	1.8	1.6	1.3	1.3	1.9	1.5	1.8	1.6	2.2	ng/g	6.5	12.2	3.4	4.0	3.9	5.8
Tm	µg/g	0.25	0.34	0.19	0.21	0.26	0.25	0.26	0.26	0.33	ng/g	0.8	3.0	1.1	1.0	1.7	1.2
Yb	µg/g	1.3	1.5	1.5	1.5	1.7	1.8	1.6	1.6	2.2	ng/g	10.5	17.5	5.8	6.0	8.8	10.7
Lu	µg/g	0.25	0.30	0.21	0.22	0.23	0.23	0.26	0.27	0.32	ng/g	2.2	3.4	1.8	2.4	2.3	2.5
Hf	µg/g	1.2	1.5	1.1	1.1	1.0	1.3	1.2	1.0	1.2	ng/g	b.d.	b.d.	2.9	1.2	b.d.	b.d.
Th	µg/g	0.43	0.45	0.43	0.43	0.35	0.46	0.43	0.31	0.39	ng/g	b.d.	0.44	b.d.	0.88	b.d.	b.d.
U	µg/g	0.088	0.12	0.12	0.10	0.11	0.11	0.12	0.091	0.12	ng/g	0.2	0.47	0.10	b.d.	0.08	0.14

[a] Used for internal standardization, determined by EPMA; b.d. below detection limit.

temperature gradient and rapid heating above the chondrule solidus to trigger partial remelting of the chondrule.

4.1.2. Olivine

Measured olivine-melt Fe/Mg exchange or apparent partition coefficients (D*) in type-I chondrules are commonly far below the expected equilibrium value of 0.3 (Roeder and Emslie, 1970). Experiments by Wick and Jones (2012), simulating type-I POP chondrule formation, also yielded small D* between 0.01 and 0.11. For MET00526_Ch43, the D* determined for the most fayalitic olivine phenocryst composition in the chondrule centre and mesostasis-1 is 0.06. Given the large range of reported D* for type-I chondrules of ~0.01–0.4 (Jones et al., 2017), it is possible (although not certain) that the olivine phenocrysts grew from a melt with a composition similar to mesostasis-1. In this case, the mesostasis-1 composition might reflect the highly differentiated primary quenched melt composition in MET00526_Ch43 prior to remelting. Smaller olivine crystals towards the periphery of the chondrule generally trend towards lower Fo contents down to Fo 90. But it should be noted that also some small forsteritic olivine grains (Fo ~94) occur towards the outer parts of the chondrule (Fig. 1f). The calculated D* for the most fayalitic olivine (Fo 90) occurring in mesostasis-2 and average mesostasis-1 is 0.11. In contrast, D* for these olivine grains and average mesostasis-2 composition is lower (0.06). Clearly all these values indicate conditions far from equilibrium. However, the highest D* obtained for fayalite-rich olivine in the outer part of the chondrule and mesostasis-1 indicates, that these crystals precipitated from a melt that was more similar to mesostasis-1 than mesostasis-2. This is also supported by continuous positive linear correlations between Fe and the incompatible minor elements Mn, Cr and Ca covering the whole compositional (Fo#) range of olivine in this chondrule (Supplementary Fig. S1). These normal magmatic trends indicate that most olivine in the two types of mesostasis in MET00526_Ch43 formed from one evolving melt and, in contrast to low-Ca pyroxene, does not record two clearly distinct mineral populations. This observation does not rule out that small amounts of olivine towards the chondrule periphery were partially remelted as well. If olivine was partially remelted as well, the amount of resorbed olivine must have been considerable smaller compared to the amount of low-Ca pyroxene.

4.1.3. Mesostasis

Generally, the compositional range of mesostasis in MET00526_Ch43 for the major elements Si, Al, Mg, Ca and Na is similar to the compositional range of mesostasis in type-I chondrules reported by Jones and Danielson (1997). Exceptions are slightly higher Na_2O concentrations in the mesostasis-2 and lower concentrations in mesostasis-1. The most significant chemical differences between the two mesostases are observed in Ca, Na, K, Cs, Rb, Sr and Eu abundances. Rubidium in mesostasis-2 is depleted (0.43 × CI) relative to mesostasis-1 (8.65 × CI) and agrees with concentrations in mesostasis of radially zoned type-I

chondrules by Grossman et al. (2002), whereas Rb concentrations in mesostasis-1 are higher than the maximum values reported in the same study, but agree with concentrations obtained on type-I chondrules from low-petrologic grade chondrites by Ruzicka et al. (2008). Caesium concentrations in both types of mesostasis fall within the range reported for a variety of barred and porphyritic olivine and pyroxene chondrules from the LL chondrites Semarkona, Chainpur and Bishunpur (Alexander, 1994). Only very few data for Rb (Alexander, 1994, Grossman et al., 2002, Ruzicka et al., 2008) and Cs (Alexander 1994) concentrations in mesostasis of type-I chondrules in UOCs have been reported so far, especially for unzoned chondrules. Alexander (1994) reported alkali zonation in mesostasis of the studied samples, but does not specifically report which of the Rb and Cs analyses were acquired from zoned chondrules and which were not. While Grossman et al. (2002) analysed zoned chondrules only, Ruzicka et al. (2008) do not describe if (some) samples were zoned or not. Thus, it remains unclear if their Rb data were (partially) acquired from zoned chondrules or not. The published Rb concentrations in mesostasis of type-I chondrules vary significantly. While values reported by Grossman et al. (2002) range from 0.1 to 3.4 × CI (in zoned chondrules), most chondrules from Alexander (1994) yield Rb contents between 0.3 and 1.8 × CI with two chondrules recording significantly higher values of 11.8 and 12.6 × CI. In contrast, most chondrules studied by Ruzicka et al. (2008) yield elevated Rb contents in the mesostasis. The average Rb content of chondrule mesostasis from the least-metamorphosed chondrite in their study (NWA 3127, LL3.1) is 8.9 × CI. Assuming that these chondrules sample random type-I chondrules they might largely be unzoned, as is the majority of type-I chondrules. If this assumption is valid, the values reported by Ruzicka et al. (2008) could be considered to best record Rb contents in unaltered type-I chondrule mesostasis. Data for Cs in type-I chondrule mesostasis are even more scarce with only a single study (Alexander, 1994) reporting Cs values ranging from 0.2 to 8.4 × CI. In that study, the sample yielding the highest Cs concentration also shows one of the highest Rb contents. Taking the Rb values from Ruzicka et al. (2008) as reference for unaltered type-I chondrules, and assuming similar behaviour of Cs and Rb during high-temperature processing of chondrules, Cs values of 8.4 × CI reported by Alexander (1994) might reflect least modified Cs compositions as well. If the two assumptions are correct, mesostasis-1 in MET00526_Ch43 has largely undepleted Rb and moderately depleted Cs concentrations, but both elements are strongly depleted in mesostasis-2.

Potassium, Rb and Cs, belong to the most volatile elements, thus their depletion in mesostasis-2 could be the result of evaporation during the partial remelting of the chondrule. However, the ca. 15-fold enrichment of Na in mesostasis-2 relative to mesostasis-1 and the sharp chemical transition between the two types of mesostasis in the alkalis and Ca, argue against a simple volatility-controlled depletion process. Alexander (1994) showed that Na in the mesostasis of type-I chondrules generally shows the poorest correlation with the other alkalis, i.e. K, Rb and Cs, and argued that Na is more mobile even during low-temperature metamorphism or aqueous alteration than the heavier alkalis. However, the strong decoupling of Na from Rb, Cs and especially K in mesostasis of MET00526_Ch43 requires a different process. Strontium and Eu both show negative anomalies in mesostasis-1 and positive anomalies in mesostasis-2, while average Eu and Sr concentrations in mesostasis of type-I chondrules from Semarkona and Bishunpur (Jacquet et al., 2015) do not show these anomalies. Sodium, K, Rb, Ba, Sr, Eu, and Ca show the strongest concentration differences between mesostasis-1 and mesostasis-2, and all of them but Ca show a strong affinity for either a silicate melt or feldspar. These elements are also highly incompatible in all other major phases in chondrules with the exception of Ca being compatible in augite or diopside. Plotting the L-chondrite normalized concentrations of these elements except Ca in both types of mesostasis reveals, that a ~3:7 mixture of mesostasis-1 and mesostasis-2 (relative area proportions deduced from the maps) results in a close to chondritic bulk mesostasis pattern with a slight negative slope towards the elements having the lower condensation temperature (Lodders, 2003) (Fig. 5a). The interpretation of this trend as a result of volatility is further supported by the order of alkali volatility over a silicic melt (Rb > K > Na) observed in experiments (Sossi et al., 2019). The relative proportions of the two types of mesostasis would change to ~2:8 if considering mostly spherical expansions of mesostasis-1 and mesostasis-2 in 3D. This has, however, only minor impact on the calculated mesostasis bulk composition (Fig. 5a). Calcium is compatible in both, plagioclase and augite, the latter occurring as late phase overgrowing low-Ca pyroxene. This complementarity indicates a genetic link between the two types of mesostasis, which sample a common precursor reservoir. Volatility-driven evaporation of K and Rb during remelting as the sole cause for their relative depletion in mesostasis-2 can therefore be excluded. Also later addition of material to the chondrule or melting of a pre-existing dust rim, as has been discussed for other samples (Krot and Wasson, 1995), is highly unlikely for this chondrule, because it would require two materials with very unusual chemical compositions (which are unknown from the literature) that coincidentally amount to a mostly chondritic bulk. Fig. 5b shows calculated apparent partition coefficients (D_i) between mesostasis-2 and mesostasis-1 and partition coefficients for Ba, K, Sr, Eu (Severs et al., 2009) and Rb (Philpotts and Schnetzler, 1970) between dacitic melt and plagioclase. The apparent partition coefficients between the two types of mesostasis are in near perfect agreement with those expected from plagioclase-melt equilibrium partitioning and thus indicate the presence of feldspar during primary chemical fractionation of melt in MET00526_Ch43. Partitioning of Ba and Eu in mesostasis-2 appears to be higher than what would be expected from the data by Severs et al. (2009). However, Ba partitioning into feldspar strongly decreases with increasing An-content (Blundy and Wood, 1991), which is consistent with the higher apparent partitioning of Ba in MET00526_Ch43 mesostasis-2 (normative plagioclase

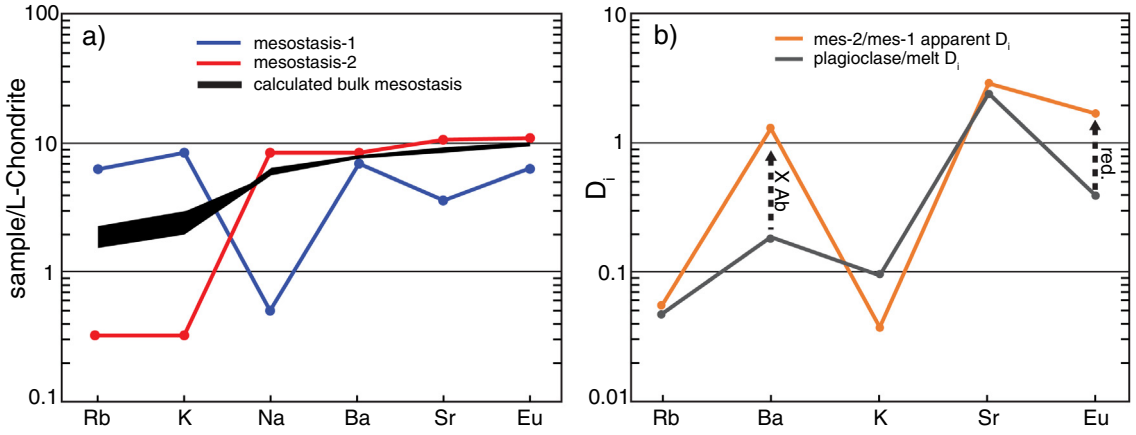

Fig. 5. (a) L-chondrite normalized (Wasson and Kallemeyn, 1988) concentrations of volatile and refractory major, minor and trace elements in chondrule MET00526_Ch43 that all show strong affinity for either silicate melt or feldspar. The black area in (a) represents the range of the calculated bulk mesostasis composition, using different relative proportions of the two types of mesostasis (see main text). The calculated mesostasis bulk composition yields a mostly flat pattern (i.e. chondritic relative abundances) with a probably volatility-controlled negative slope towards Rb, the more volatile elements (Lodders, 2003). This complementarity of mesostasis-1 and mesostasis-2 indicates a common precursor for the two different types of mesostasis and suggests largely closed system behaviour during partial remelting. (b) Apparent partition coefficients (D_i) for mesostasis-2/mesostasis-1 show very good agreement with measured plagioclase/melt D_i (Severs et al., 2009; Philpotts and Schnetzler, 1970). Major deviations of apparent D_i to measured D_i for Ba and Eu are caused by differences in feldspar compositions and redox conditions.

$Ab_{80}An_{20}$) compared to the more calcic plagioclase analysed by Severs et al. (2009). Partitioning of Eu into feldspar strongly depends on the oxidation state of Eu and thus the redox environment during crystallization (Drake and Weill, 1975). The relatively higher apparent partition coefficient of Eu is thus caused by the reducing conditions during chondrule formation.

The presence of feldspar in chondrites is commonly associated with thermal metamorphism, during which it can form by recrystallization of matrix material or, in chondrules, by crystallization of glassy mesostasis (e.g. Van Schmus and Wood, 1967; Grossman and Brearley, 2005; Huss et al., 2006). Some studies have reported the rare occurrence of feldspar interpreted to have formed by crystallization from the chondrule melt (e.g. Russell et al., 2000; Huss et al., 2001). In a recent study, Lewis and Jones (2018) described and discussed the occurrence of feldspar in ferromagnesian type-I and type-II chondrules and concluded that about 20% of the investigated Semarkona chondrules contain feldspar that crystallized from melt as *primary phase* during chondrule formation. In most of the described porphyritic chondrules, plagioclase is not homogeneously distributed throughout the whole chondrule and is commonly associated with remnant glassy mesostasis. In the Fe-poor POP chondrule Ch3, described in detail by Lewis and Jones (2018), plagioclase occurs within glassy mesostasis predominantly in the outer part of the chondrule and not in the centre. These findings are in line with the observation that crystallization of feldspar has played an important role for the chemical fractionation of mesostasis in MET0052_Ch43. This is also supported by Raman analysis performed in different patches of mesostasis-1 and mesostasis-2 that yield indications of feldspar in mesostasis-2, which is also texturally different to glassy mesostasis-1 (Fig. 2a-c). The two most prominent plagioclase bands at ~480 and ~510 cm^{-1} are both recorded in mesostasis-2, while they are absent in mesostasis-1 (Fig. 6). The 320 and 675 cm^{-1} peaks in mesostasis-2 can be attributed to diopside, a common micro-crystallite in mesostasis, although a prominent diopside peak above

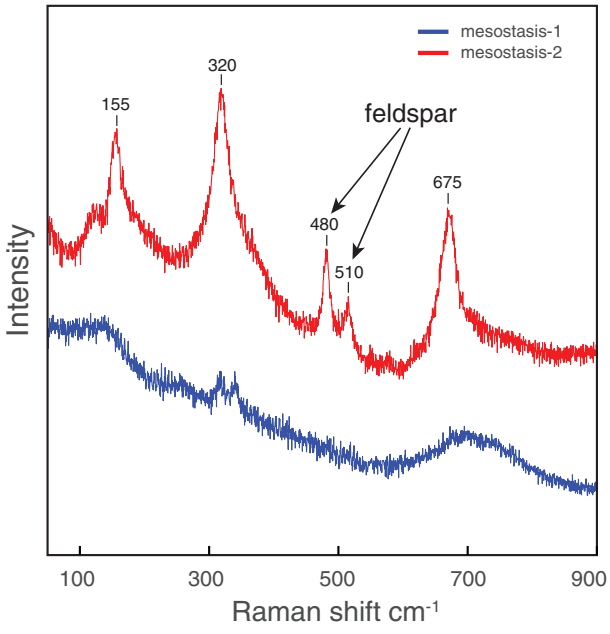

Fig. 6. Raman spectra measured in mesostasis-1 and mesostasis-2 of chondrule MET00526_Ch43. The two most prominent feldspar bands at ~480 and ~510 cm^{-1} are visible in mesostasis-2 and are absent in mesostasis-1. Raman peaks at 320 and 675 cm^{-1} could be attributed to diopside crystallites in the mesostasis.

1000 cm^{-1} has not been detected. Collectively, the plagioclase normative composition ($Ab_{80}An_{20}$) of mesostasis-2, the strong evidence for plagioclase-controlled fractionation of Rb, Na, K, Ba, Sr and Eu in combination with the identification of feldspar in mesostasis-2 by Raman analysis clearly show, that feldspar crystallization, predominantly in the outer parts of the chondrule, was the main controlling process for chemical fractionation of the melt during primary chondrule formation. The sharp chemical transition between mesostasis-1 and mesostasis-2 that is apparent in some parts of the chondrule and the clear chemical dichotomy of mesostasis in MET00526_Ch43 must have developed after the partial remelting of the chondrule, by homogenisation of the melt/mesostasis in the outer part due to melting (mesostasis-2) and possibly some diffusive homogenisation of the mesostasis-1 in the inner parts of the chondrule.

4.1.4. Sequence of mesostasis fractionation and remelting

The element abundances in mesostasis-1 and mesostasis-2 require that feldspar crystallized in a late-stage melt during the first chondrule forming event. In contrast, the distribution of the two low-Ca pyroxene generations, of which the second generation clearly formed after (or due to) remelting, indicates that remelting only affected some parts of the chondrule. It is therefore unlikely that the feldspar-controlled fractionation of melt in MET00526_Ch43 (Figs. 1, 5) was caused by the remelting event, because this must have been a disequilibrium process, possibly due to the short reheating. Additionally, the generally increasing Fa-content in olivine towards the chondrule rim (with few exceptions) together with the decreasing olivine grain size (Fig. 1f) implies that most of the olivine must have formed by continuous fractional crystallization during primary chondrule formation. Slow cooling of the primary chondrule melt led to the formation of large olivine phenocrysts in the chondrule centre and incipient enrichment of incompatible elements in the remaining melt towards the chondrule periphery. Crystallization of plagioclase during cooling began mostly in the outer parts of the chondrule, leading to a strong chemical fractionation of the remaining melt. Reheating and remelting must have been rapid processes, failing to achieve complete equilibrium in the chondrule. The melting degree, as is indicated by the distribution of low-Ca pyroxene gen-1 and gen-2, was not high enough in order to remelt larger parts in the chondrule centre. This prevented homogenization of the whole mesostasis but enhanced the chemical gradient in the mesostasis and eventually led to the sharp chemical boundary between mesostasis-1 and mesostasis-2. The subsequent cooling of the partly molten chondrule was rapid, since large-scale diffusive reequilibration between mesostasis-1 and mesostasis-2 is lacking.

4.2. Remelting of chondrule MET00452_Ch22

Similar to chondrule MET00526_Ch43, also the type-I chondrule MET00452_Ch22 records evidence for partial remelting after primary formation. In contrast to MET00526_Ch43, this chondrule displays a continuous zonation of Na, K and Ca in the mesostasis from the centre to the periphery. These chemical trends are similar to those observed in many type-I chondrules from UOCs (Matsunami et al., 1993; Grossman et al., 2002), where Na, K, Rb and Cs increase systematically towards the chondrule rim while Ca shows the opposite trend. Matsunami et al. (1993) interpreted this zonation (in a single chondrule) to have been caused by the reduction of dusty precursor material and recondensation of volatile elements onto the chondrule surface during or subsequent to chondrule formation, while fractional crystallization within the chondrule or transport of volatile elements into the chondrule during aqueous alteration were considered unlikely scenarios. In contrast, Grossman et al. (2002) systematically studied several zoned type-I chondrules from Semarkona in great detail for their major, minor and some trace element systematics, including H contents. Some of the analysed chondrules show identical zonation trends as the chondrule described by Matsunami et al. (1993), while other chondrules show different patterns. They note that the evolutionary history of zoned type-I chondrules might be too complex to explain all different observed features in concentrically zoned type-I chondrules by a single process, but ultimately argue in favor of low-temperature aqueous alteration on the chondrite parent body to have been the major cause for modification of type-I chondrule mesostasis. Noteworthy is that they also discuss that some observations could indeed point towards high-temperature reprocessing or partial remelting after primary formation and prior to alteration on respective parent bodies. The most striking differences between MET00452_Ch22 and the chondrules studied by Grossman et al. (2002) are the generally higher concentrations of Na_2O and MnO and the flat profiles for Al and Si abundances throughout the mesostasis in the sample studied here. Additionally, while Ca concentrations vary by only few tens of % in the Grossman et al. (2002) samples, Ca concentrations in MET00452_Ch22 mesostasis show a significantly larger range and increase by a factor of 4–5. Silicon and Al show varying trends in the Semarkona chondrules but they almost always anticorrelate. In MET00452_Ch22 mesostasis Si concentrations systematically increase from core to rim by ~5% relative, but Al contents are largely constant throughout the mesostasis. Yet, the overall similarity of MET00452_Ch22 with the chondrules described by Grossman et al. (2002) implies that similar processes modified these chondrules.

In addition to the radial zonation of Na, K and Ca in mesostasis, MET00452_Ch22 shows a textural feature, which it has in common with MET00526_Ch43, and which has not been described before by Grossman et al. (2002) or Matsunami et al. (1993): The MnO concentration map for low-Ca pyroxene (Fig. 4f) reveals two texturally (and partially chemically) different types of low-Ca pyroxene. This observation is very similar to what has been described above for MET00526_Ch43. Low-Ca pyroxene in MET00452_Ch22 has a bimodal grain size distribution. Systematically smaller low-Ca pyroxene grains occur solely in the chondrule centre around large olivine phenocrysts, whereas the outer part of the chondrule is dominated by

large euhedral low-Ca pyroxene crystals. The small low-Ca pyroxene grains in the chondrule centre display chemically distinct relict cores with significantly higher Mn, Ca and Cr contents. These trends are similar but less pronounced than what is observed in MET0056_Ch43. A systematic change in Mg# between the two types of low-Ca pyroxene, as is clearly observed in MET00526_Ch43, is difficult to evaluate from the chemical maps, but is, if present, much less pronounced in MET00452_Ch22 as well. As has been argued for MET00526_CH43, partial remelting seems to be the best explanation for the two distinct low-Ca-pyroxene generations in both samples. The two low-Ca pyroxene populations in chondrule Met00452_Ch22 suggest that also this chondrule was remelted early in its history. Compared to MET00526Ch43, remelting in MET00452_Ch22 must have been more extensive, because larger low-Ca pyroxene cores (gen-1) are missing even in the chondrule centre.

Although this chondrule does not record conclusive evidence for feldspar crystallization during primary formation, the distribution of alkalis + Eu as well as varying molar proportions of Al and Si in the mesostasis might indicate the local presence of feldspar prior to the chondrule remelting. The observed variable pattern of these elements in the mesostasis of MET00452_Ch22 could consequently be related to a complete local remelting of primary feldspar but incomplete equilibration of these melts during chondrule remelting.

4.3. Chondrule remelting: An asymmetric process?

From the different chemical maps of the two partially remolten chondrules (Figs. 1, 4) it is evident that both samples record an additional striking feature. The remolten paragenesis in both samples does not occur concentrically around the primary inner zones of the chondrules, but shows an asymmetric distribution.

This could indicate that the two studied chondrules have been non-symmetrically abraded, probably during the accretion into their parent bodies (Kitamura and Watanabe, 1986; Liffman, 2019). An alternative explanation is that remelting in both samples was highest at the chondrule periphery, but melt formation appears to have affected the chondrules outermost parts to different degrees within the individual chondrules. This asymmetric distribution of the second melt may indicate uneven heating of the chondrule outer layers due to directed, anisotropic heating. This must have resulted in a strong temperature gradient not only between the outermost parts of the chondrule and the chondrule centre, but also between the chondrule front oriented toward the heat pulse and its respective shadow side. This supports an asymmetric and directed process delivering the required energy for chondrule remelting.

4.4. Constraints on the timing of chondrule remelting

Partial remelting of chondrules during a second heating event could modify the primary abundances of the volatile elements and the mineral assemblages of individual chondrules. If and to which degree a chondrule behaves as an open system depends on many parameters (e.g. peak temperature, duration of heating, chondrule size, chondrule environment). Chondrule reprocessing during high-temperature events consequently has important implications for the interpretation of the chemical composition of bulk chondrules and of chondrule ages. Partial remelting can fractionate the Al/Mg ratio in the mesostasis and this way resets or disturbs the primary ^{26}Al-^{26}Mg ages of chondrules obtained from the analysis of mesostasis and coexisting minerals. Partial remelting of Mg-rich low-Ca pyroxene and/or late formation of high-Al diopside preferentially in the remolten area of the chondrule can change the Al/Mg ratios in the mesostasis, which affects the resulting ^{26}Al-^{26}Mg ages of chondrules. ^{26}Al-^{26}Mg ages obtained from partially remolten chondrules must therefore be carefully evaluated to ascertain their significance and to minimize the risk of misinterpretation of such dates. While no age information is available for MET00526_Ch43, a ^{26}Al-^{26}Mg age has previously been determined for chondrule MET00452_Ch22 (Pape et al., 2019). Al-Mg isotopes in this chondrule have only been measured in the remolten paragenesis, i.e. the mesostasis and large euhedral low-Ca pyroxenes grains occurring in the outer part of the chondrule (Fig. 4a). The chondrule records the youngest ^{26}Al-^{26}Mg age ($2.92^{+0.75}_{-0.43}$ Ma) of all 31 UOC chondrules analysed by Pape et al. (2019) and likely dates the time, when (the outer) parts of the chondrule got remolten. Although having large uncertainties, this age is analytically resolved from the gross of chondrule ages around ~2 Ma after CAIs and can thus be interpreted to date a late and distinct high-temperature event in the protoplanetary disk occurring at ~3 Ma after CAIs, rather than the primary formation of the chondrule. This implies that multiple, distinct thermal pulses occurred in the chondrule forming region of the protoplanetary disk throughout the time interval of chondrule formation (i.e. 1.8–3 Ma, Villeneuve et al., 2009; Pape et al., 2019). During this time interval the chondrules must have remained suspended and accretion of the parent body of this chondrite did not finalize before ~3 Ma after CAIs.

5. SUMMARY AND CONCLUSIONS

Chemical and textural systematics in mesostasis and mafic silicates of two type-I chondrules yield evidence for multiple crystallization and melting processes in single chondrules prior to incorporation in their respective parent body. Chemical and mineralogical features reveal a first melting event that was followed by partial crystallization of the chondrule melt involving olivine, low-Ca pyroxene and also feldspar. During a later short-lived thermal pulse in the protoplanetary disk some chondrules were partially remelted.

The unique Fe-poor chondrule MET00526_Ch43 preserves chemical, mineralogical and textural signatures that trace various stages of this multi-stage thermal history from primary formation to subsequent reheating and partial remelting under more reducing conditions in the protoplanetary disk. Chemical and textural relationships of two low-Ca pyroxene generations occurring in the inner and outer part of the chondrule, including partial resorption of the

first-generation pyroxene and non-oscillatory repetition of elemental zoning, require a high temperature event that led to partial remelting of this chondrule. This melting event was associated with the formation of metallic Fe, now found irregularly distributed along the former melt-crystal interfaces, which implies a lower oxygen fugacity for the remelting process than for the primary chondrule formation. The remelting dominantly affected the outer parts of the chondrule, in which the mesostasis was originally enriched in primary feldspar that had fractionated the late melt during primary chondrule formation and led to chemical gradients within the mesostasis. The primary feldspar in the mesostasis together with low-Ca pyroxene (and probably some olivine) in the outermost parts partially melted during a subsequent brief high-temperature thermal pulse, which was followed by rapid cooling and crystallization of the second generation of low-Ca pyroxene. The innermost parts of the chondrule and most olivine grains throughout the chondrule were largely unaffected by this partial remelting. Evaporative loss of volatile elements from the bulk chondrule during this high-temperature event affected mostly Rb and K. High-temperature reprocessing by partial remelting also affected the Fe-poor chondrule MET00452_Ch22 but the degree of remelting must have been more extensive as compared to chondrule MET00526_Ch43. The second melting event(s) that affected these individual chondrules must have occurred prior to incorporation of the chondrules into the chondrite parent body as both samples are of low petrographic type and did not exceed temperatures in excess of ~300 °C after accretion. The two types of melt and newly formed minerals thus provide evidence for multiple high temperature pulses that led to reprocessing of chondrules prior to accretion in a planetesimal. Thus, chondrule formation in the solar nebula is not a single thermal event but the consequence of multiple punctuated thermal events that achieved temperatures significantly above the solidus of the mineral assemblage in some chondrules. The asymmetry in the second-generation melt implies a directed thermal pulse.

The observation of primary crystallization mechanisms as well as partial remelting processes preserved in the studied chondrules indicate that the chondrule forming process was dynamic and involved several discrete thermal pulses in a chemically evolving environment. Chondrules that formed by a single melting event and chondrules showing evidence for multiple melting occur in the same chondrite sample. This implies that the second thermal pulse that partially melted some chondrules might have been more localized than the first event. The mineralogical and textural relationships are furthermore not consistent with chondrule formation as a consequence of planetesimal collision of (partially) molten bodies (e.g. Lichtenberg et al., 2018) as this would produce rather a single thermal pulse followed by formation of chondrules from the ejected material. The age span of ca. 1.2 Myr observed between pristine chondrules and chondrules affected by high-temperature reprocessing provides thus firm time constraints on the duration of the chondrule forming process. The spread in ages found in all chondrules from CC and UOC meteorites (e.g. Villeneuve et al. 2009, Pape et al., 2019) does not necessarily imply a continuous process of chondrule formation, but is consistent with several thermal pulses that reached temperatures high enough to partially remelt pre-existing chondrules. The age constraints combined with the petrographic features of some chondrules imply that chondrules remained suspended in the protoplanetary disk from ca. 1.8–3.0 Ma after CAI formation.

Declaration of Competing Interest

The authors declare that they have no known competing financial interests or personal relationships that could have appeared to influence the work reported in this paper.

ACKNOWLEDGEMENTS

We would like to thank the ANSMET meteorite working group (MWG) for providing the samples MET 00452 and MET 00526 from the NASA Collection of Antarctic Meteorites. We would like to thank M. Robyr for access to the EPMA facility at the Institute of Earth Sciences, University of Lausanne and S. Ebert and A. Bischoff for access and support at the SEM facility at Institut für Planetologie, Universität Münster.

Constructive reviews by A. Ruzicka, R. Jones and one anonymous reviewer improved the quality of this manuscript. We also would like to thank S. Russell for the editorial handling of the manuscript.

This work has been carried out in the framework of the NCCR PlanetS supported by the Swiss National Science Foundation grant nr. 51NF40-141881.

APPENDIX A. SUPPLEMENTARY MATERIAL

Supplementary data to this article can be found online at https://doi.org/10.1016/j.gca.2020.10.019.

REFERENCES

Akaki T., Nakamura T., Noguchi T. and Tsuchiyama A. (2007) Multiple formation of chondrules in the early solar system: chronology of a compound Al-rich chondrule. *Astrophys. J. Lett.* **656**, L29.

Alexander C. M. O., Barber D. and Hutchison R. (1989) The microstructure of Semarkona and Bishunpur. *Geochim. Cosmochim. Acta* **53**, 3045–3057.

Alexander C. M. O. (1994) Trace element distributions within ordinary chondrite chondrules: Implications for chondrule formation conditions and precursors. *Geochim. Cosmochim. Acta* **58**, 3451–3467.

Baecker B., Rubin A. E. and Wasson J. T. (2017) Secondary melting events in Semarkona chondrules revealed by compositional zoning in low-Ca pyroxene. *Geochim. Cosmochim. Acta* **211**, 256–279.

Blundy J. D. and Wood B. J. (1991) Crystal-chemical controls on the partitioning of Sr and Ba between plagioclase feldspar, silicate melts, and hydrothermal solutions. *Geochim. Cosmochim. Acta* **55**, 193–209.

Bollard J., Connelly J. N., Whitehouse M. J., Pringle E. A., Bonal L., Jørgensen J. K., Nordlund Å., Moynier F. and Bizzarro M.

(2017) Early formation of planetary building blocks inferred from Pb isotopic ages of chondrules. *Sci. Adv.* **3**(8), e1700407.

Connolly, Jr, H. C., Hewins R. H., Ash R. D., Zanda B., Lofgren G. E. and Bourot-Denise M. (1994) Carbon and the formation of reduced chondrules. *Nature* **371**, 136.

Drake M. J. and Weill D. F. (1975) Partition of Sr, Ba, Ca, Y, Eu2+, Eu3+, and other REE between plagioclase feldspar and magmatic liquid: an experimental study. *Geochim. Cosmochim. Acta* **39**, 689–712.

Guillong M., Meier D. L., Allan M. M., Heinrich C. A. and Yardley B. W. (2008) Appendix A6: SILLS: A MATLAB-based program for the reduction of laser ablation ICP-MS data of homogeneous materials and inclusions. *Mineral. Assoc. Canada Short Course* **40**, 328–333.

Grossman J. N., Alexander C. M. O., Wang J. and Brearley A. J. (2002) Zoned chondrules in Semarkona: Evidence for high- and low-temperature processing. *Meteorit. Planet. Sci.* **37**, 49–73.

Grossman J. N. and Brearley A. J. (2005) The onset of metamorphism in ordinary and carbonaceous chondrites. *Meteorit. Planet. Sci.* **40**, 87–122.

Hanon P., Robert F. and Chaussidon M. (1998) High carbon concentrations in meteoritic chondrules: A record of metal-silicate differentiation. *Geochim. Cosmochim. Acta* **62**, 903–913.

Hewins R. H. (1997) Chondrules. *Annu. Rev. Earth Planet. Sci.* **25**, 61–83.

Hewins R., Connolly H., Lofgren Jr G. and Libourel G. (2005) Experimental constraints on chondrule formation. In: Chondrites and the protoplanetary disk, vol. 341, 286.

Huss G. R., MacPherson G. J., Wasserburg G., Russell S. S. and Srinivasan G. (2001) Aluminum-26 in calcium-aluminum-rich inclusions and chondrules from unequilibrated ordinary chondrites. *Meteorit. Planet. Sci.* **36**, 975–997.

Huss G. R., Rubin A. E. and Grossman J. N. (2006) Thermal metamorphism in chondrites. *Meteorit. Early Sol. Syst. II* **943**, 567–586.

Jacquet E., Alard O. and Gounelle M. (2015) Trace element geochemistry of ordinary chondrite chondrules: The type I/type II chondrule dichotomy. *Geochim. Cosmochim. Acta* **155**, 47–67.

Jones R. H. (1994) Petrology of FeO-poor, porphyritic pyroxene chondrules in the Semarkona chondrite. *Geochim. Cosmochim. Acta* **58**, 5325–5340.

Jones R. H. (1996) FeO-rich, porphyritic pyroxene chondrules in unequilibrated ordinary chondrites. *Geochim. Cosmochim. Acta* **60**, 3115–3138.

Jones R. H. (2012) Petrographic constraints on the diversity of chondrule reservoirs in the protoplanetary disk. *Meteorit. Planet. Sci.* **47**, 1176–1190.

Jones R. H. and Danielson L. R. (1997) A chondrule origin for dusty relict olivine in unequilibrated chondrites. *Meteorit. Planet. Sci.* **32**, 753–760.

Jones R., Villeneuve J. and Libourel G. (2017) Thermal histories of chondrules: Petrologic observations and experimental constraints. In: Chondrules and the Protoplanetary Disk, LPI Contribution No 1963, id 2029.

Kita N. T., Nagahara H., Togashi S. and Morishita Y. (2000) A short duration of chondrule formation in the solar nebula: evidence from ^{26}Al in Semarkona ferromagnesian chondrules. *Geochim. Cosmochim. Acta* **64**, 3913–3922.

Kitamura M. and Watanabe S. (1986) Adhesive growth and abrasion of chondrules during the accretion process. In Memoirs of the National Institute of Polar Research. The Tenth Symposium on Antarctic Meteorites, Proceedings of the 1985 conference, vol. 41 (eds. K. Yanai, H. Takeda and A. Shimoyama). Springer, pp. 222–234.

Krot A. N. and Wasson J. T. (1995) Igneous rims on low-FeO and high-FeO chondrules in ordinary chondrites. *Geochim. Cosmochim. Acta* **59**, 4951–4966.

Krot A. N. and Rubin A. E. (1996) Microchondrule-bearing chondrule rims: constraints on chondrule formation. Chondrules and the protoplanetary disk (ed. RH Hewins, RH Jones Sz ERD Scott), 181-184.

Krot A. N., Rubin A. E., Keil K. and Wasson J. T. (1997) Microchondrules in ordinary chondrites: Implications for chondrule formation. *Geochim. Cosmochim. Acta* **61**, 463–473.

Lanari P., Vidal O., De Andrade V., Dubacq B., Lewin E., Grosch E. G. and Schwartz S. (2014) XMapTools: A MATLAB©-based program for electron microprobe X-ray image processing and geothermobarometry. *Comput. Geosci.* **62**, 227–240.

Lewis J. A. and Jones R. H. (2018) Primary feldspar in the Semarkona LL 3.00 chondrite: Constraints on chondrule formation and secondary alteration. *Meteorit. Planet. Sci.* **54**, 72–89.

Lichtenberg T., Golabek G. J., Dullemond C. P., Schönbächler M., Gerya T. V. and Meyer M. R. (2018) Impact splash chondrule formation during planetesimal recycling. *Icarus* **302**, 27–43.

Liffman K. (2019) Fine-grained rim formation–High speed, kinetic dust aggregation in the early Solar System. *Geochim. Cosmochim. Acta* **264**, 118–129.

Lodders K. (2003) Solar system abundances and condensation temperatures of the elements. *Astrophys. J.* **591**, 1220.

Marrocchi Y., Villeneuve J., Batanova V., Piani L. and Jacquet E. (2018) Oxygen isotopic diversity of chondrule precursors and the nebular origin of chondrules. *Earth Planet. Sci. Lett.* **496**, 132–141.

Matsunami S., Ninagawa K., Nishimura S., Kubono N., Yamamoto I., Kohata M., Wada T., Yamashita Y., Lu J., Sears D. W. G. and Nishimura H. (1993) Thermoluminescence and compositional zoning in the mesostasis of a Semarkona group A1 chondrule and new insights into the chondrule-forming process. *Geochim. Cosmochim. Acta* **57**, 2101–2110.

McDonough W. F. and Sun S.-S. (1995) The composition of the Earth. *Chem. Geol.* **120**, 223–253.

Pack A. and Palme H. (2003) Partitioning of Ca and Al between forsterite and silicate melt in dynamic systems with implications for the origin of Ca, Al-rich forsterites in primitive meteorites. *Meteor. Planet. Sci.* **38**, 1263–1281.

Pape J., Mezger K., Bouvier A.-S. and Baumgartner L. (2019Pack) Time and duration of chondrule formation: Constraints from ^{26}Al-^{26}Mg ages of individual chondrules. *Geochim. Cosmochim. Acta* **244**, 416–436.

Philpotts J. A. and Schnetzler C. (1970) Phenocryst-matrix partition coefficients for K, Rb, Sr and Ba, with applications to anorthosite and basalt genesis. *Geochim. Cosmochim. Acta* **34**, 307–322.

Roeder P. and Emslie R. (1970) Olivine-liquid equilibrium. *Contrib. Mineral. Petr.* **29**, 275–289.

Rubin A. E., Trigo-Rodrıguez J. M., Huber H. and Wasson J. T. (2007) Progressive aqueous alteration of CM carbonaceous chondrites. *Geochim. Cosmochim. Acta* **71**, 2361–2382.

Rubin A. E. (2010) Physical properties of chondrules in different chondrite groups: Implications for multiple melting events in dusty environments. *Geochim. Cosmochim. Acta* **74**, 4807–4828.

Russell S. S., MacPherson G. J., Leshin L. A. and McKeegan K. D. (2000) ^{16}O enrich-melts in aluminum-rich chondrules from ordinary chondrites. *Earth Planet. Sci. Lett.* **184**, 57–74.

Russell S. S., Connolly, Jr., H. C. and Krot A. N. (2018) *Chondrules. Records of protoplanetary disk processes*. Cambridge University Press.

Ruzicka A., Hiyagon H., Hutson M. and Floss C. (2007) Relict olivine, chondrule recycling, and the evolution of nebular oxygen reservoirs. *Earth Planet. Sci. Lett.* **257**, 274–289.

Ruzicka A., Floss C. and Hutson M. (2008) Relict olivine grains, chondrule recycling, and implications for the chemical, thermal, and mechanical processing of nebular materials. *Geochim. Cosmochim. Acta* **72**, 5530–5557.

Scott E. R. D. and Taylor G. J. (1983) Chondrules and other components in C, O and E chondrites: Similarities in their properties and origins. In *Proceedings of the 14th Lunar and Planetary Science Conference J. Geophys. Res.*, 88 (Suppl.), pp. B275–B286.

Sears D. W. G., Morse A. D., Hutchison R., Guimon R. K., Jie L. u., Alexander C. M. O'D., Benoit P. H., Wright I., Pillinger C., Xie T. and Lipschutz M. E. (1995) Metamorphism and aqueous alteration in low petrographic type ordinary chondrites. *Meteoritics* **30**, 169–181.

Severs M. J., Beard J. S., Fedele L., Hanchar J. M., Mutchler S. R. and Bodnar R. J. (2009) Partitioning behavior of trace elements between dacitic melt and plagioclase, orthopyroxene, and clinopyroxene based on laser ablation ICPMS analysis of silicate melt inclusions. *Geochim. Cosmochim. Acta* **73**, 2123–2141.

Sossi P. A., Klemme S., O'Neill H. S. C., Berndt J. and Moynier F. (2019) Evaporation of moderately volatile elements from silicate melts: experiments and theory. *Geochim. Cosmochim. Acta* **260**, 204–231.

Tomeoka K. and Buseck P. R. (1990) Phyllosilicates in the Mokoia CV carbonaceous chondrite: Evidence for aqueous alteration in an oxidizing environment. *Geochim. Cosmochim. Acta* **54**, 1745–1754.

Ushikubo T., Nakashima D., Kimura M., Tenner T. J. and Kita N. T. (2013) Contem- poraneous formation of chondrules in distinct oxygen isotope reservoirs. *Geochim. Cosmochim. Acta* **109**, 280–295.

Van Schmus W. and Wood J. A. (1967) A chemical-petrologic classification for the chondritic meteorites. *Geochim. Cosmochim. Acta* **31**, 747–765.

Villeneuve J., Chaussidon M. and Libourel G. (2009) Homogeneous distribution of ^{26}Al in the solar system from the Mg isotopic composition of chondrules. *Science* **325**, 985–988.

Wasson J. T. and Kallemeyn G. W. (1988) Compositions of chondrites. *Phil. Trans. R. Soc. Lond. A* **325**, 535–544.

Wasson J. T. and Krot A. N. (1994) Fayalite-silica association in unequilibrated ordinary chondrites: Evidence for aqueous alteration on a parent body. *Earth Planet. Sci. Lett.* **122**, 403–416.

Wick M. J. and Jones R. H. (2012) Formation conditions of plagioclase-bearing type I chon-drules in CO chondrites: A study of natural samples and experimental analogs. *Geochim. Cosmochim. Acta* **98**, 140–159.

Associate editor: Sara S. Russell